Front. Environ. Sci. Eng. 2024, 18(8): 93
https://doi.org/10.1007/s11783-024-1853-y

REVIEW ARTICLE

A review of CFD simulation in pressure driven membrane with fouling model and anti-fouling strategy

Shiyong Miao[1], Jiaying Ma[1], Xuefei Zhou[1,2], Yalei Zhang[1,2], Huaqiang Chu (✉)[1,2]

1 State Key Laboratory of Pollution Control and Resource Reuse, Tongji University, Shanghai 200092, China
2 Shanghai Institute of Pollution Control and Ecological Security, Tongji University, Shanghai 200092, China

HIGHLIGHTS

- The numerical realization method of the membrane permeation process is summarized.
- Biofouling, scaling and colloidal particle fouling models are detailed presented.
- Representative CFD-aided simulations of anti-fouling strategies are described.

ARTICLE INFO

Article history:
Received 25 December 2023
Revised 22 February 2024
Accepted 21 March 2024
Available online 10 May 2024

Keywords:
Computational fluid dynamics
Membrane
Fouling model
Concentration polarization

GRAPHIC ABSTRACT

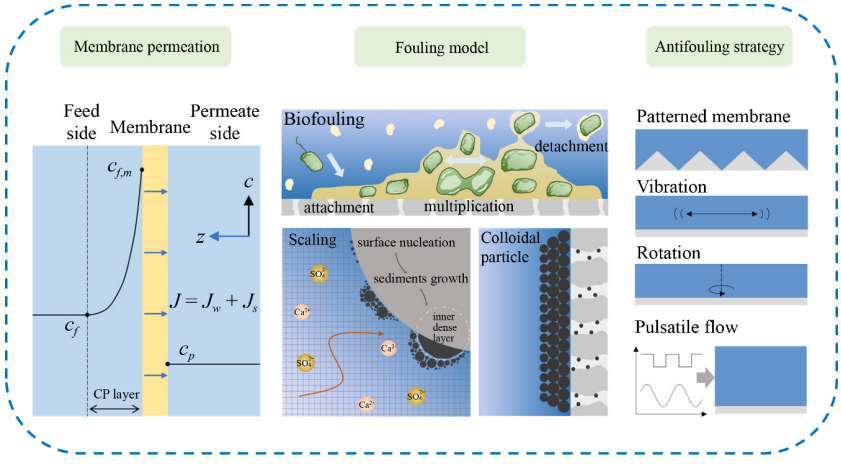

ABSTRACT

Pressure-driven membrane filtration systems are widely utilized in wastewater treatment, desalination, and water reclamation and have received extensive attention from researchers. Computational fluid dynamics (CFD) offers a convenient approach for conducting mechanistic studies of flow and mass transfer characteristics in pressure-driven systems. As a signature phenomenon in membrane systems, the concentration polarization that accompanies the permeation process is a key factor in membrane performance degradation and membrane fouling intensification. Multiple fouling models (scaling, biofouling and colloidal particle fouling) based on CFD theory have been constructed, and considerable research has been conducted. Several representative antifouling strategies with special simulation methods, including patterned membranes, vibration membranes, rotation membranes, and pulsatile flows, have also been discussed. Future studies should focus on refining fouling models while considering local hydrodynamic characteristics; experimental observation tools focusing on the internal structure of inhomogeneous fouling layers; techno-economic model of antifouling strategies such as vibrational, rotational and pulsatile flows; and unfavorable hydraulic phenomena induced by rapidly changing flows in simulations.

1 Introduction

Due to the challenging global water crisis, pressure-driven membrane separation technologies have gained widespread adoption worldwide. Their applications include seawater and brackish water desalination; municipal, industrial, and agricultural wastewater treatment and reclamation; and tap water purification (Wei et al., 2021; Johnston et al., 2022; Lin et al., 2022b). The popularity of these membrane technologies can be attributed to their high efficiency, outstanding effluent quality, stable operation, and relatively low energy consumption.

✉ Corresponding author
E-mail: chuhuaqiang@tongji.edu.cn

The membrane separation system encounters various challenges in practical applications, and the following two steps are of utmost importance. (i) Concentration polarization (CP): CP leads to a substantial increase in solute concentration around the membrane surface, resulting in elevated energy consumption and reduced membrane module yield due to permeability reduction. Additionally, CP increases the risk of scaling and shortens the lifespans of membranes (Johnston et al., 2022). (ii) Concomitant membrane fouling: Membrane fouling can be classified into several different categories including biofouling, particulate and colloidal fouling, inorganic fouling (scaling), and organic fouling.

CFD has been extensively utilized as an auxiliary tool in theoretical research and in the product design of membrane systems, resulting in a growing body of associated literature. Researchers have studied the performance optimization and fouling control of membrane filtration systems from several perspectives with the help of CFD tools. Classification by foulant type includes scaling (Radu et al., 2014a; Uppu et al., 2020), biofouling (Kostoglou and Karabelas, 2013; Cao et al., 2018; Jeong et al., 2020; Kerdi et al., 2021; Desmond et al., 2022), and colloidal particle fouling (Uppu et al., 2019). Classification by antifouling strategies includes optimization of the spacer geometry (Han et al., 2018; Kavianipour et al., 2019; Ruiz-García and de la Nuez Pestana, 2019; Xie et al., 2019; Toh et al., 2020), patterned membranes (surface roughness) (Shang et al., 2020b; 2020a; Zhou et al., 2021), vibration membranes (Lorente et al., 2018; Su et al., 2019; Tan et al., 2019), rotation membranes (Jogdand and Chaudhuri, 2015; Uppu et al., 2019; Park et al., 2023), and pulsation feeds (Zoubeik et al., 2018; Salama et al., 2020; Li et al., 2022; 2023). Furthermore, the simulation scope was expanded from several localized repeating spacer cells to full-scale membrane devices (Mao et al., 2021; Wei et al., 2021; Lin et al., 2022a). As a well-established numerical simulation technique, the effectiveness of CFD within membrane systems has been widely validated (Liang et al., 2020; Chong et al., 2023).

There have been reviews in the field of membrane fouling with various focuses. Membrane performance optimization strategies involving spacer geometry optimization (Haidari et al., 2018; Lin et al., 2021; Rahmawati et al., 2021) and surface modification (Asadollahi et al., 2017; Wang et al., 2023) have gained considerable attention. The membrane fouling theory and corresponding anti-fouling strategies have also been well reviewed (Bucs et al., 2018; Goh et al., 2018; 2019; Jamieson and Leterme, 2021; Najid et al., 2022). In addition, studies have focused on specific membrane types, such as FOs (Liang and Fletcher, 2023), membranes with electromagnetic fields (Piyadasa et al., 2017), and spiral wound membrane (SWM) modules (Karabelas et al., 2015). Notably, CFD simulation results have served as key evidence, whereas the simulation methodology has received limited attention and lacked comprehensive evidence, despite numerous studies coupling different fouling models that have emerged in recent years.

In this paper, a comprehensive review of studies concerning simulations of membrane modules using CFD is provided, which encompasses the theoretical background and modeling approaches of these systems. In contrast to existing reviews, this work prioritizes how CFD numerical simulations of membrane systems are conducted, specifically the numerical implementation of the membrane permeation process and concentration polarization and the method of coupling fouling models. Moreover, several representative antifouling strategies with special simulation methods, including patterned membranes, vibration membranes, rotation membranes, and pulsatile flows, are also mentioned.

2 CFD basic theory

The governing equations including continuity (or mass), momentum (Navier–Stokes), and solute mass transport (convection–diffusion) equations are utilized to describe the conservation and transport processes:

$$\rho\nabla\cdot\mathbf{v}=\boldsymbol{S}_{m1}, \tag{1}$$

$$\rho\left(\frac{\partial\mathbf{v}}{\partial t}+\mathbf{v}\cdot\nabla\mathbf{v}\right)=-\nabla p+\nabla\cdot\left(\overline{\overline{\tau}}\right)+\boldsymbol{S}_{m2}, \tag{2}$$

$$\frac{\partial c}{\partial t}+\mathbf{v}\cdot\nabla\mathrm{c}=D\nabla^2 c+\boldsymbol{S}_{m3}, \tag{3}$$

where $\overrightarrow{v}$ is the velocity vector, ρ is the fluid density, p is the hydraulic pressure, $\overline{\overline{\tau}}$ is the stress tensor, c is the solute concentration and D is the solute diffusivity. The source terms $\boldsymbol{S}_{m1}$, $\boldsymbol{S}_{m2}$, and S_{m3} are presented in the following text. For example, if the effect of gravity is considered, then $\boldsymbol{S}_{m2}=\rho\boldsymbol{g}$. The item $\nabla\cdot\left(\overline{\overline{\tau}}\right)$ is replaced by $\mu\nabla^2\boldsymbol{v}$ in most studies. The effect of volume dilation $\mu\nabla^2\boldsymbol{v}-\frac{2}{3}\nabla\cdot\boldsymbol{v}\boldsymbol{I}$ has also been considered in many studies. Many researchers have adopted turbulence models, such as the renormalization group (RNG) k–ε model (Bahoosh et al., 2022), standard k–ε model (Park et al., 2021), shear stress transport (SST) model (Mokhtar et al., 2021), large eddy simulation (LES) model (Su et al., 2018), and direct numerical simulation (DNS) (Ali et al., 2020). Additionally, the fluid viscosity μ is replaced by $1/Re$ (Re is the Reynolds number) (Wu and Lin, 2012; Kerdi et al., 2018; 2020), while the diffusion coefficient D is replaced by vH/D (v is the fluid velocity, H is the feed channel height) (Koutsou et al., 2018). In this paper, Re refers to the Reynolds number, v represents the fluid velocity and H represents the height of the feed channel. Definitions of dimensionless numbers including Re, Sh, Sc, Pn, and

other metrics commonly used in CFD (e.g., shear stress and mass transfer coefficient) are provided in the Supplementary Material. Table 1 details the geometric structure, simulation parameter settings, and key results in the CFD modeling of the membrane modules. Notably, the governing equations are applied in the fluid domain, while the spacers are assumed to be in a noninteracting solid domain. Due to the complexity of the geometry, the spacer is considered as a porous domain in some studies to replace its blocking effect on the flow by setting the source term $\boldsymbol{S}_{m2} = -\mu\mathbf{v}/\kappa_{\text{spacer}} - 0.5\text{R}_{\text{spacer}}\rho\mathbf{v}|\mathbf{v}|$ in Eq. (2) and the parameter values used in the spacer porous domain are presented in Table 2.

Several common assumptions are made to simplify complex flow and mass transfer systems (Evangelista, 1988; Boudinar et al., 1992). The fluid is assumed to be a constant-density, incompressible Newtonian fluid. The flow is considered steady and laminar. Additionally, in most studies, changes in concentration, pressure, velocity, and osmotic pressure on the permeate side are neglected due to minimal foulant retention and stable pressure guaranteed by atmospheric pressure. The permeate side hardly affects the membrane performance, so the feed side is preferred for the simulation domain.

3 Membrane permeation and concentration polarization

Mass transport through osmotic membranes is a critical mechanism in filtration systems and requires prudence in numerical simulations. According to Darcy's law, the permeate flux J can be calculated by Eq. (4), and the permeable membrane is numerically determined by setting the source term at the boundary wall, as shown in Eq. (5):

$$J = \frac{1}{R\mu}(\Delta P - \Delta\pi), \tag{4}$$

$$\boldsymbol{S}_{m1} = -J\rho A/V\boldsymbol{j}, \tag{5}$$

where R is the permeation resistance, μ is the viscosity of the solution, P is the pressure, π is the osmotic pressure and Δ is the difference between the membrane sides. A is the face area adjacent to the membrane, and V is the volume adjacent to the membrane. $\boldsymbol{j}$ is the normal vector perpendicular to the membrane. The components $\frac{1}{R\mu}$ can be replaced by the water permeability L_w. The permeation resistance R commonly comprises three components: the membrane inherent resistance R_m, the concentration polarization resistance R_{cp}, and the fouling resistance R_f. R_m is typically treated as a constant, while R_{cp} is associated with the concentration polarization effect. The magnitude and composition of R_f vary depending on the type of fouling, such as scaling, colloidal fouling or biofouling. These aspects are discussed in the following sections. Item $\Delta\pi$ can be omitted because the osmotic pressure is negligible in comparison to the transmembrane pressure (Sablani et al., 2001). In studies where inorganic salts are the target foulant, the osmotic pressure is controlled by the solute concentration and can be derived from the modified van't Hoff formula:

$$\pi = N_{ion}RTc, \tag{6}$$

where N_{ion} is the ionization number, R is the gas constant and T is the temperature. Table 3 lists the detailed correlations between c and π, as well as the fluid density, viscosity and diffusion coefficient.

The concentration polarization (CP) is widespread and extremely important to consider in numerical simulations of pressure-driven membrane systems. As membrane permeation intensifies, water enters the permeation channel, while a substantial amount of solute (e.g., salt and dissolved substrate) becomes trapped on the feed side. The convection-diffusion process fails to uniformly distribute solute in the bulk flow over time, resulting in the formation of a thin CP layer near the membrane surface. This phenomenon may cause the concentration between the membrane surface and the bulk flow to differ by up to three times (Completo et al., 2016). A high concentration at the membrane surface increases the osmotic pressure π and reduces the net pressure ($\Delta P - \Delta\pi$) difference, thus weakening the driving force for membrane permeation. The CP layer ultimately contributes to the promotion of membrane fouling and reduces membrane performance. Another perspective reveals that according to the equation ($\delta_v/\delta_c \text{ Sc}^{1/3}$), the thickness of the viscous boundary layer δ_v (i.e., the region of sharply reduced fluid velocity near the wall) significantly exceeds that of the concentration boundary layer δ_c (Li et al., 2016). This finding suggests that the flow velocity within the concentration boundary layer is influenced primarily by the wall rather than by the bulk flow. Such observations underscore the importance of boundary layer flow field disturbances.

As depicted in Fig.1, a notable concentration disparity exists between the bulk flow and the membrane surface, and these differences can be connected through the CP model (Schock & Miquel, 1987; Senthilmurugan et al., 2005):

$$\frac{C_{f,m} - C_p}{C_f - C_p} = e^{J/k}, \tag{7}$$

where C_f is the bulk feed concentration of salt, C_p is the bulk permeate concentration of salt, $C_{f,m}$ is the feed concentration of salt at the membrane surface and k is the mass transfer coefficient.

The experimentally obtained R_{cp} can be used to macroscopically analyze the effect of CP on filtration systems. The salt water and pure water are filtered under the same operating conditions, and the difference in the total permeate resistance calculated from Eq. (4) is R_{cp}.

Table 1 Summary of CFD simulations about SWM modules

Spacer geometry	Feature size	Flow state & Boundary condition	Mesh & Software	Validation	Significant results or innovation point	Ref.
3D; 3 × 5 cells nonwoven, 2-layer, nonuniform spacer	$H = 0.78$ mm; $W = 78$ mm; $L_m = 2.85$ mm; $D_f = 386 - 555$ μm; $\alpha = 45°$; $\beta = 90°$	$Re = 127$; Laminar $u_0 = 0.163$ m/s nonpermeable membrane	$N = 430000$ Tetrahedron; $S < 200$ μm COMSOL 3.5	Not mentioned	First 3D model for biofouling in the feed channel	Picioreanu et al. (2009)
2D (1) Submerged spacer (2) Zigzag spacer (3) Cavity spacer	$D_f = 500$ μm; $W = 1$ mm; $L = 15$ mm; $L_m = 4$ mm	$Re = 160$; Laminar; Steady $u_0 = 0.1$ m/s permeable membrane	$N = 200000 - 270000$ $S = \begin{cases} 5 - 30\ \mu m \\ 10\ \mu m\ for\ biofilm\ mesh \end{cases}$ COMSOL 3.5	Literature	Spacer geometry is based on (Schwinge et al., 2002a); Biofouling model is developed based on (Picioreanu et al., 1998a, 2001); Potential biofouling area is suggested.	Radu et al. (2010; 2012)
3D; Sinusoidal spacers	$H = 1.5$ mm; $W = 6$ mm Wavelength = 12, 24 mm	$u_0 = 0.148$ m/s permeable membrane	510–640 elements/mm^3 COMSOL 4.2	Original experiment	Permeate is enhanced by the sinusoidal channel.	Xie et al. (2014)
3D; 5 cells (1) Commercial spacers (2) 2-layer, nonwoven, nonuniform spacer	$D_f = 221 - 563$ μm $H = 711 - 1168$ μm $L = 2385 - 2788$ μm $\alpha = 45°$; $\beta = 90°$ Porosity: 0.88 – 0.92	$Re < 200$; Laminar Stationary in each biomass calculation time step $u_0 = 0.041 - 0.178$ permeable membrane	$N = 1300000$ $S < 90$ μm tetrahedral mesh COMSOL 4.3	Original experiment and literature (Araújo et al., 2012; Vrouwenvelder et al., 2009b)	Biofouling model is developed based on (Picioreanu *et al.*, 2009); The influence of the nutrient load, spacer geometry, work condition on biofouling in NF is investigated.	Bucs et al. (2014a; 2014b)
3D; 1 cell 2-layer, nonwoven, nonuniform spacer	$\alpha = 45°, 90°$; $\beta = 90°$ $H = 800$ μm; $L = 4411$ μm $W = 4411$ μm $D_f = 250 - 520$ μm $L_m \approx 3100$ μm	Laminar; Steady $u_0 = 0.14$ m/s permeable and nonpermeable membrane for different cases	S < 30 μm Tetrahedral COMSOL 4.2	Original experiments	Particle trajectory is used to determine the potential fouling area, and the cross-velocity has an effect on the deposition area.	Radu et al. (2014b)
3D; 1 cell 2-layer, nonwoven, nonuniform spacer	$W = 4.38$ mm; $L = 4.38$ mm $H = 787$ μm; $\beta = 90°$	$Re = 70, 160, 300$ Steady; Laminar $u_0 = 74, 163, 294$ mm/s nonpermeable membrane	S < 50 μm Tetrahedral COMSOL 4.4	Original experiments	Simulation with different velocities has been induced in SWM modules and exhibits in good agreement with experiments.	Bucs et al. (2015)
2D; zigzag	$L = 15$ mm; $H = 1$ mm $L_m = 4$ mm; $D_f = 0.5$ mm	Laminar; Steady; $u_0 = 0.07 - 0.2$ m/s permeable membrane	$S < 5$ μm COMSOL 3.5	Not mentioned	A model integrating mineral precipitation and biofilm formation with hydrodynamics and solute transport is developed, and the interactions between biofouling and scaling is investigated.	Radu et al. (2015)
3D; 1 cell (1) 2-layer, nonwoven, uniform spacer (2) 1-layer, uniform, spherical node spacer	$D_{node}/D_f = 2$ $L_m/D_f = 10, 12$ $\beta = 105°$, 120°	$Re < 200$; Flow state depended on Re $Sc = 1 - 100$ nonpermeable membrane with constant wall concentration	Not mentioned Fluent 6.2	Original experiment	Spherical spacer node reduced contact area with membrane significantly.	Koutsou & Karabelas (2015)

(*Continued*)

Spacer geometry	Feature size	Flow state & Boundary condition	Mesh & Software	Validation	Significant results or innovation point	Ref.
3D; five mesh angles (1) Nonwoven spacer; 1 cell (2) Partially woven spacer; 1 cell (3) Middle layer spacer; 1 cell (4) Fully woven spacer; 2 cells	H = 1 mm; L_m = 4.5 mm D_f = 0.5, 1 mm α = 30°, 60°,90° β = 30°, 60°, 90°	Re_{ch} = 224 Laminar; Steady u_0 = 0.1 m/s permeable membrane	N = 1.4–2.9 million Tetrahedral COMSOL 5.0	not mentioned	3D simulations of 20 spacer geometries with considering realistic boundary condition via the solution-diffusion model.	Gu et al. (2017)
3D; 9 cells (1) Zigzag spacer (2) Triple spacer (3) Wavy spacer	D_f = 0.5 mm; H = 1 mm $L = W$ = 4.1 mm (1.5 mmfortriplespacer) α = 90°; β = 90°	Re = 50200 Steady; Laminar Nonpermeable membrane with a constant wall concentration of 35% w/w NaCl	Tetrahedral S > 0.1 μm Fluent 15,16	Li et al.,（2004）; Shakaib et al.,（2007); Saeed et al., 2012	Correlations of various parameters with Re is developed and compared with other studies; Comparison of spacer geometries based on pressure drop, SCE, SPC, Pn, Sh and other performance indicators.	Kavianipour et al. (2017)
2D; 35 cells; Zigzag spacer	D_f = 0.39 mm; H = 0.78 mm L = 200 mm; L_m = 2.85 mm	LES turbulence model permeable membrane	$N = 6.8\times10^5$ S > 0.8 μm Fluent	Original experiment	Time-dependent salt concentration distribution and permeate flux in a vibrating membrane system is obtained	Su et al. (2018)
3D; 1 cell 2-layer, nonwoven, uniform spacer	$H = 2D_f$; L_m/D_f = 8 α = 45°; β = 90°	Re = 60 – 200; Flow state depended onRe Sc = 1 – 100 DNS (direct numerical simulation) Nonpermeable membrane with constant wall concentration	Not mentioned Fluent 6.2	Literature (Koutsou et al., 2007)	Assuming a uniform fouling layer on the membrane surface.	Koutsou et al. (2018)
3D; 2 cells + 2 half cells 1-layer, uniform spacer with 0-3 holes;	H = 1200 μm L_m = 4000 μm D_f = 1000 μm α = 45°; β = 90° Hole diameterD_{hole} = 300,500 μm	Re = 73 – 375 Q_0 = 12 L/h nonpermeable membrane	22 million grid points Fluent	Original experiment with synthetic solution	3D model for 3 novel feed spacers with perforations.	Kerdi et al. (2018)
3D; 3 cells 2-layer, nonwoven, nonuniform spacer	H = 787 μm L_m = 3100 μm D_f = 340 – 610 μm α = 45°; β = 90°	steady to unsteady; DNS (direct numerical simulation) nonpermeable membrane	67 million grid points Fluent 17	Original experiment	Overlap at the intersection of filaments	Qamar et al. (2019)
3D; 3 cells Nonwoven, uniform filament with 2-layer or 3-layer	H = 1 mm D_f/H = 0.4 – 0.6 L_m/H = 4 α = 0 – 60°; β = 90°	Re_h = 200; Steady Sc = 600 Permeable membrane	N = 90 million Tetrahedral CFX 16.2 nonstructured cells with a maximum size of 3% – 5%H in main fluid domain prismatic cells with a size of 2% – 4%H and a minimum number of 20 for the inflated boundary	Literature (Fimbres-Weihs & Wiley, 2007; Schwinge et al., 2002b; 2004)	Multiscale techno-economic model for feed spacer channel in RO system is established	Liang et al. (2019)

(*Continued*)

Spacer geometry	Feature size	Flow state & Boundary condition	Mesh & Software	Validation	Significant results or innovation point	Ref.
3D; 1 × 4 cells (1) Empty (2) Circular spacer (3) Diamond spacer (4) Elliptic spacer	–	u_0 = 0.1, 0.3, 0.5 m/s Standard k–ε model	N = 3886000 Hexahedral dominant Fluent 6.3	Original experiment	The great potential to mitigate membrane fouling and enhance permeate flux of turbulence promoter, especially the elliptic shape, is confirmed.	Tsai et al. (2019)
3D Nonwoven, uniform spacer with standard nodes or column nodes	H = 1.2 mm $D_f = \begin{cases} 0.5\ \text{mm (colum spacer)} \\ 1\ \text{mm (standard spacer)} \end{cases}$ L_m = 4 mm; D_{node} = 1.5 mm $\alpha = 45°$; $\beta = 90°$	u_0 = 0.16, 0.18 m/s Unsteady; Nonpermeable membrane	N = 30 million Fluent 2018	Original experiment	Better performance such as pressure drop reduction, shear stress reduction and higher specific flux is found for novel column spacer compared to standard spacer.	Ali et al. (2019)
3D; 1 × 3 cells (1) Standard spacer (2) Turbo spacer	–	DNS (direct numerical Simulation) Nonpermeable membrane	Hexahedron dominant	Original experiment	Novel turbo spacer exhibits better performance in facilitating the homogenous distribution of high velocity and shear stress compared to a standard spacer.	Ali et al. (2020)
3D; 3 × 5 cells (1) 2-layer, nonwoven, nonuniform spacer (2) 1-layer, nonuniform spacer	H = 460 μm $L_m = \begin{cases} 1770\ \mu m for 2 layer \\ 3140\ \mu m for 1 layer \end{cases}$ $D_f = \begin{cases} 220-320\ \mu m 2 layer \\ 280-460\ \mu m 1 layer \end{cases}$ $\alpha = 45°$; $\beta = 90°$	u_0 =0.12 m/s Steady; Laminar Nonpermeable membrane	2.3 million grids	Original experiment	Nonuniform filament with different thinning zone location (0, 1/3, 1/2) on filaments.	Lin et al. (2020)
2D (1) Cavity spacer (2) Submerged spacer (3) Zigzag spacer	L_m/D_f = 4, 8, 12 H = 0.2 – 1.4	Steady; Laminar Permeable membrane	N = 9000 – 16200 COMSOL 5.1	Literature (Schock & Miquel, 1987; Koutsou et al., 2009)	Correlation for CP; pressure drop is concluded.	Gu et al. (2021)
3D; 2 cells 1-layer, pillar nodes, uniform filament	H = 1200 μm D_f = 340, 500, 1000 μm $\alpha = 45°$; $\beta = 90°$ D_{node} = 1000 μm	u_0 = 92, 185, 389, 469 mm/s Transient; Laminar nonpermeable membrane	Fluent	Original experiment	Same numerical methodology with (Kerdi et al., 2018).	Kerdi et al. (2021)
3D; 3 cells; Single layer (1) Commercial, nonuniform spacer (2) Pillar node, uniform spacer (3) Hole pillar, uniform spacer	L = 20 mm; H = 1.2 mm L_m = 4 mm; D_{node} = 1 mm D_f = 0.5 *or* 0.5 – 0.9 mm Hole: 0.4 mm × 0.25 mm $\alpha = 45°$; $\beta = 90°$	u_0 = 0.185 m/s Nonpermeable membrane	hexahedral S > 50 μm ~2600000 grid points Fluent 2020	Original experiment	Measuring parameters in intermediate units to avoid inlet and outlet effects.	Qamar et al. (2021)
3D; 1 cell 2-layer, fully woven, uniform spacer	$D_f = H/1.8$ $\alpha = 45°$; $\beta = 90°$ Porosity: 0.663 – 0.828	Re > 400; shear stress transport (SST) turbulence model nonpermeable membrane	N = 6000220 – 13714094 Tetrahedral mainly, with tetrahedra and prisms in the regions surrounding the filaments. S/H = 2, 3, 4	Literature	Flow, mass transfer and heat transfer are simulated; The dependence of f, Nu andSh on the Reynolds number shows a double asymptotic trend; The attack angle and filament spacing have significant influence on flow and mass/heat transfer.	Mokhtar et al. (2021)

(*Continued*)

Spacer geometry	Feature size	Flow state & Boundary condition	Mesh & Software	Validation	Significant results or innovation point	Ref.
3D (1) Standard spacer; 1 × 3 cells (2) Honeycomb-shaped spacer; 1 × 2 cells	(1)$\alpha = 45°$; $\beta = 90°$ $L_m = 2.79$ mm; $D_f = 0.43$ mm (2)$\alpha = 30°$; $\beta = 120°$ $L_m = 1.73$ mm; $D_f = 0.4$ mm	$Re = 295.74$;Steady Standard k–ε model	N =33, 20 million	Original experiment	Honeycomb spacer increases the permeate flux, mitigates CP, and inhibits fouling layer deposition.	Park et al. (2021)
3D; 3 × 5 cells 2-layer, nonwoven, uniform filament	$D_f = 0.4 - 0.6$ mm $H = 660 - 864$ μm $L_m = 2 - 4$ mm $\alpha = 15 - 37.5°$; $\beta = 30 - 90°$ Porosity: 0.630 – 0.882	$Re < 300$; Laminar $u_0 = 0.12$ m/s Nonpermeable membrane	N =12.9_22.7 million	Original experiment	Channel porosity is one of the determinant parameters for spacer performance and the appropriate value is approximately 0.85.	Lin et al. (2022b)
3D; 2 × 6 cells (1) 2-layer, nonwoven, uniform spacer (2) 2-layer, fully woven, uniform spacer (3) 2-layer, nonwoven, uniform, spine ramp spacer	$H = 0.77$ mm; $W = 3.465$ mm; $L_m = 1.2, 1.5$ mm; $D_f = 385$ μm; $\alpha = 45, 60°$; $\beta = 90, 60°$	Re ≈ 300; realizable k–ε turbulence model $u_0 = 0.2$ m/s permeable membrane	N =3.2_5.8 million Tetrahedral S = 14 – 45 μm	Literature	High membrane flux aggravates CP; Water flux, solute flux, CP modulus, pressure drop and wall shear rate are used in spacer performance evaluation.	Bae et al. (2023)

Note: The meanings of the symbols in the table are shown below: α is the attack angle, β is the mesh angle, D_f is the filament diameter, H is the channel height, L_m is the filament spacing and W is the channel width. D_{node} is the diameter of the spacer nodes, N is the mesh number and S is the mesh size.

Table 2 Parameters in the spacer porous domain

Parameter	κ_{spacer}	R_{spacer}	ε
	Permeability coefficient for the porous spacer	Resistance loss/inertial coefficient for the porous spacer	Porosity for the porous spacer
unit	m^2	m^{-1}	–
Lin et al. (2022a)	2×10^{-9} [i]	25775 [i]	0.8
Abdelkader & Sharqawy (2022)	0.97×10^{-8}–64.85×10^{-8} [ii]	33–282.9	0.74–0.89
Jeong et al. (2020)	2×10^{-10}	–	0.5

Table 3 Calculation correlations of permeation parameters

Solute	Osmotic pressure $\Delta\pi$ (bar)	Viscosity μ (Pa·s)	Diffusion coefficient D (m^2/s)	Density ρ (kg·m^3)	Ref.
1 mg/L $MgSO_4$	$4.97\times10^5\, m(49.55-136.7\, m+1207\, m^2)$	$0.8972\times10^{-3}(1+3.713\, m+26.0614\, m^2)$	$0.849\times10^{-9}(1-0.41873\, m^{0.0872})$	$997+1036\, m$	Yang et al. (2023)
<100 g/L NaCl	$77.17\, m$				Johnston et al. (2023)
< 0.09 kg/kg NaCl	$805.1\times10^5\hat{m}$	$0.89\times10^{-3}(1+1.63\hat{m})$	$\mathrm{Max}\begin{cases}(1.61\times10^{-9}(1-14m)\\1.45\times10^{-9}\end{cases}$	$997.1\times(1.0+0.696\, m)$	Cao et al. (2018); Guan et al. (2023); Shang et al. (2021)
$0.1 < c < 1.5$ mol/L NaCl	$4.793\times10^6 c$	$10^{-3}(1.004+0.08c)$	1.45×10^{-9}	$995.7+38.54c$	Su et al. (2018)
$c < 0.6$ mol/L $CaCl_2$	$(62.35c + 13.14c^2+8.993c^3)\times10^5$	$10^{-3}(1.004 + 0.2981c)$	$\begin{cases}(1.176+107.5c)/(1+95.24c+26.03c^2)for c<0.132\\1.134-0.3213c+0.2319c^2-0.1553c^3\, for 0.132<c<0.6\end{cases}$	$995.7+89.72c$	
$c < 0.6$ mol/L Na_2SO_4	$(56.29c-28.37c^2+23.05c^3)\times10^5$	$10^{-3}(1.004+0.4094c)$	$\begin{cases}(1.08+129.3c)/(1+124.5c+40.92c^2)for c<0.108\\1.042-0.3225c+0.1048c^2-0.07547c^3\, for 0.108<c<0.6\end{cases}$	$995.7+11.91c$	
$0.05 < c < 0.5$ mol/L $MgSO_4$	$(33.08c–178.9c^2+942.7c^3)\times10^5$	$10^{-3}(1.004+0.06092c)$	$0.7288–0.1929c+0.1517c^2–0.9297c^3$	$995.7+11.88c$	
	$8.48\times10^4 m(0.917+2.13\times10^{-4}m+3.141\times10^{-6}m^2)$	$-6.196\times10^{-10}m^2+1.968\times10^{-6}m+9.885\times10^{-4}$	$2.811\times10^{-20}m^4-2.645\times10^{-17}m^3+7.021\times10^{-15}m^2-1.458\times10^{-13}m+1.477\times10^{-9}$	$-2.179\times10^{-4}\, m^2+0.692\, m+997.99$	Sitaraman & Battiato (2022)
Typical value for brackish desalination and softening	4.872×10^6c				Zhou et al. (2021)
BSA solution	$\pi = RT(2\sqrt{2.5\times10^{-7}Z^2c^2+c_s^2}-2c_s+10^{-3}c+10^{-6}A_2c^2M+10^{-9}A_3c^3M^2)$ $Z=-497.512-37.913pH+2896.079pH^{-2}+352.129\ln(pH)$ $A_2=-5.625\times10^{-4}-2.41\times10^{-4}Z-3.664\times10^{-5}Z^2$ $A_3=-2.95\times10^{-5}-1.051\times10^{-6}Z+1.762\times10^{-7}Z^2$	$\mu_w e^{2.44\times10^{-11}c^2}$	$D_{id}\frac{\mu_w}{\mu(c)}\sqrt{\frac{1}{RT}\frac{\partial\pi}{\partial c}}$	Constant	Schausberger et al. (2009)

Where m is the solute *m*ass concentration (mg/L), $\hat{m}$ is the solute *m*ass fraction (kg/kg), c is the solute *m*ole concentration (mol/L), c_s is the salt concentration (mol/L), M is the *m*ole *m*ass of BSA (Da, g/mol), D_{id} is the diffusion coefficient at infinite dilution and μ_w is the water viscosity.

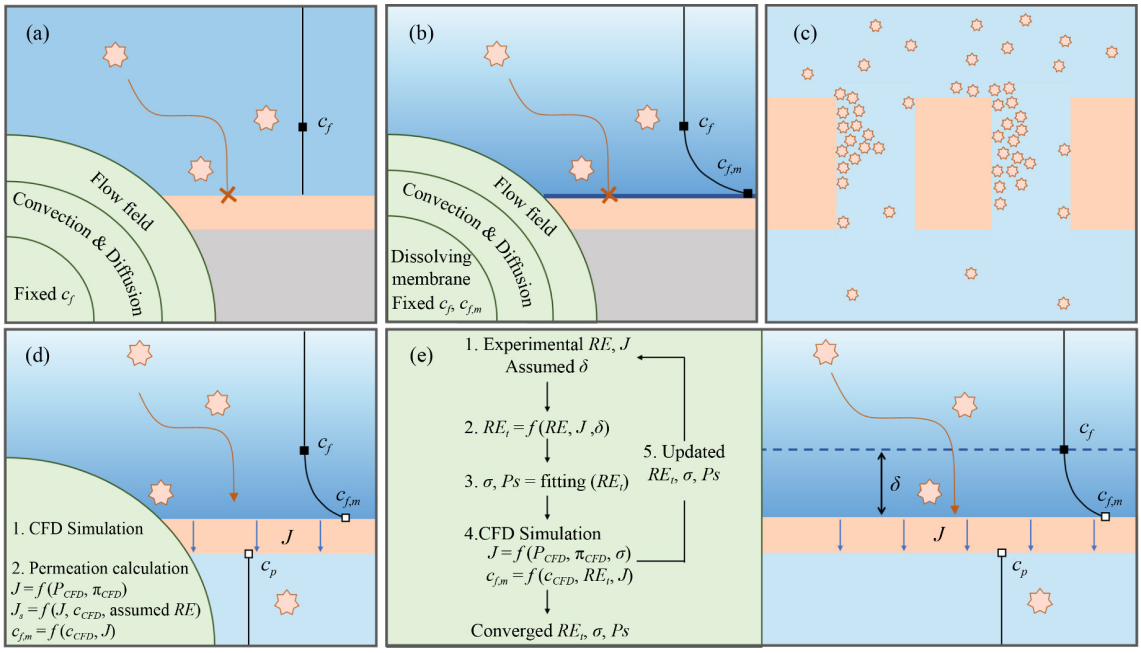

Fig. 1 Schematic of the calculation method of the permeation process and concentration near the membrane: (a) impermeable membrane; (b) impermeable and dissolving membrane; (c) construction of the membrane hole; (d) permeable membrane with direct calculation methods and (e) permeable membrane with the loop-fitting calculation method.

Schausberger et al. reported that R_{cp} accounts for 40% of the total permeate resistance and noted that the current fouling model may underestimate the impact of CP (Schausberger et al., 2009).

Pressure-driven membranes are typically classified into microfiltration (MF), ultrafiltration (UF), nanofiltration (NF), and reverse osmosis (RO) depending on the pore size. Various membrane types serve distinct functions based on filtration effectiveness and economic factors. MF/UF membranes are commonly utilized for filtration of particles (Movahedi and Jamshidi, 2022), microalgae (Kim et al., 2015), macromolecules (Sioutopoulos and Karabelas, 2012), etc., whereas RO/NF membranes are predominantly employed for desalination (Sweity et al., 2013). Consequently, the former primarily addresses particle deposition and cake layer development in CFD simulations, while the latter places greater emphasis on solute concentration. Nevertheless, this differentiation is not rigid. For instance, Shang et al. (2022b) examined colloidal particle fouling on patterned nanofiltration membranes, and Jalilvand et al. (2014) investigated the impact of concentration polarization in microfiltration systems. In essence, the choice of simulation method is dictated by specific research objectives rather than the type of membrane.

There are several ways to calculate permeation process and concentration distribution. The schematic is shown in Fig.1:

(i) Impermeable membrane

The assumption of impermeability is adopted because of its lower computational performance consumption and minimal impact on mass transfer, wall shear, and hydraulic characteristics despite its physical accuracy. Numerous studies (Cao, 2001; Ndinisa et al., 2005; Vrouwenvelder et al., 2009c; 2009a) have shown that membrane permeation contributes only minimally to mass transfer in the flow channel, estimated at approximately 0.05% per spacer cell (Qamar et al., 2019) or lower than 0.6% (Xie et al., 2014). Additionally, the permeate flow rate is extremely low, typically approximately 10 μm/s (Kerdi et al., 2020). Similarly, the ratio of the Sherwood number (Sh) simulated with permeable membranes to that simulated with impermeable membranes ranges from 1.033–1.083; This indicates that the effect of permeable walls on mass transfer is relatively insignificant (Koutsou et al., 2009; Koutsou and Karabelas, 2015).

(ii) Impermeable and dissolving membrane

To reduce the computational burden with minimal distortion of simulation accuracy and to emphasize the high solute concentration near the wall caused by concentration polarization, the method of dissolving membrane is adopted, i.e., a constant concentration value is set at the membrane surface and the membrane is considered as non-permeable (Chong et al., 2022; García-Picazo et al., 2023). This method is particularly suitable for studying the effect of obstructions in a flow channel, such as feed spacers and turbulence promoters, on flow and mass transfer. Completo et al. (2016) confirmed that the dissolving membrane method coupled with semiempirical correlation demonstrates fairly consistent results with the permeable membrane method but at the

cost of considerably less computation time. However, Binger and Achilli (2023) noted out that the constant wall concentration assumption fails to accurately describe the phenomenon in which the concentration boundary layer decreases significantly with increasing flow velocity and enhanced mixing efficacy in fluid domains.

(iii) Permeable membrane with direct calculation methods

Solutes pass through the membrane pores into the permeate channel and the solute flux J_s is corrected by the defined intrinsic rejection coefficient $RE = 1 - c_p/c_f$(99%) (Anqi et al., 2015), which is expressed through the source term $\boldsymbol{S}_{m3}$ in Eq. (3):

$$\boldsymbol{S}_{m3} = -J_s A/V\boldsymbol{j}, \tag{8}$$

$$J_s = (1-RE)Jc. \tag{9}$$

Guan et al. (2023) considered the concentration difference across the membrane in Eq. (10):

$$J_s = L_s(m_f - m_p). \tag{10}$$

Luo et al. (2020) combined Eq. (9) and Eq. (10):

$$J_s = L_s(m_f - m_p) - (1-RE)(m_f + m_p)J/2. \tag{11}$$

Based on the solute concentration in permeate channel ($c_p = J_s/JMW$, MW is the molecular weight), a further development was made (Singh et al., 2022; Bae et al., 2023):

$$J = (L_w P - L_w\pi - L_s + \sqrt{(L_w P - L_w\pi + L_s)^2 + 4L_w L_s\pi})/2, \tag{12}$$

$$J_s = L_s c_f MW(L_w P + L_w\pi + L_s - \sqrt{(L_w P - L_w\pi + L_s)^2 + 4L_w L_s\pi})/2\pi L_w, \tag{13}$$

where L_s is the solute permeability, m is the solute mass concentration and c is the solute mole concentration. The suffix f, p represent the feed channel and permeate channel, respectively.

(iv) Permeable membrane with the loop-fitting calculation method

In contrast to the direct calculations described above, Cao et al. (2018) used a loop-fitting method to calculate the parameters of the permeation process based on the Spiegler–Kedem model. First, the rejection coefficient RE and permeate flux J are experimentally measured. Second, the true rejection coefficient RE_t is calculated with the estimated CP layer thickness δ by Eq. (14). Third, the reflection coefficient σ and salt permeability Ps are calculated via nonlinear two-parameter fitting based on Eq. (15). Fourth, a CFD simulation is performed, and the refined flux J' and solute concentration on the membrane surface $c_{f,m}$ are calculated by Eqs. (16) and (17). Here, δ' represents the height of the first mesh at the membrane. Finally, since J is updated by J', RE_t' is recalculated, and further, σ' and Ps' are refitted. These corrected parameters are returned to the second step for recalculation. The above calculation loop continues until the differences between J', σ' and Ps' and between J, σ and Ps are small enough.

$$RE_t = \frac{e^{J\delta/D}RE}{1 + (e^{J\delta/D} - 1)RE}, \tag{14}$$

$$RE_t = 1 - \frac{1-\sigma}{1 - \sigma e^{-(1-\sigma)J/Ps}}, \tag{15}$$

$$J = L_w(\Delta P - \sigma\Delta\pi), \tag{16}$$

$$c_{f,m} = \frac{c_f e^{J\delta'/D}}{RE_t + (1 - RE_t)e^{J\delta'/D}}. \tag{17}$$

(v) Construction of the membrane hole

A more direct approach is to construct the geometry of the membrane pore channels. Bräsel et al. (2023) simulated the deposition process of polystyrene particles with a diameter of 5 μm on a polydimethylsiloxane (PDMS) membrane with a pore diameter of 20 μm in a cross-flow system; the results reveal an excellent fit for the fluxes in the pore channels via simulation of the intermediate pore-blocking model of Hermia's theory. However, the feasibility of this approach for accessing membranes with pore sizes less than 1 μm, which are more commonly used in water treatment processes, needs to be further investigated. Moreover, microscale simulations of membrane pores are computationally intensive.

4 Fouling model

The concentration distribution of salt (e.g., NaCl) is particularly valuable because it can aid researchers in identifying areas with high fouling potential. However, this approach has significant shortcomings in that it fails to reveal the influence of hydrodynamics on the deposition of colloidal particles, biofilm development, and inorganic salt scaling, and it also fails to explain the flux decline with severe fouling and the synergistic effect between different fouling types. Consequently, models applicable to different fouling mechanisms have been developed.

4.1 Scaling

The scaling model introduces a solubility product equation based on the concentration distribution and consequently achieves inorganic salt deposition, which affects the permeation process and hydrodynamics in membrane modules.

Two sets of meshes exist in parallel in the simulation domain, one for deposited particle simulations and the other for traditional fluid calculations. The former is predivided, while the latter is dynamically adjusted according to the biomass subdomain. The data exchanged between the two meshes are passed by interpolation. In practical scenarios, deposition does not occur

immediately even in a supersaturated state due to solution meta-stability. Hence, the critical deposition point in the simulation is $DS = 1.5$, and the solute is consumed by the source term S_{m3}, as described in Eq. (3) (Zhang & Klapper, 2010; Radu et al., 2014a):

$$S_{m3} = -k_s a_v \left(\sqrt{DS} - 1\right)^2, \tag{18}$$

$$DS = \frac{\gamma_{Ca^{2+}} \cdot \gamma_{SO_4^{2-}}}{K_{sp}} a_{H_2O} C_{salt}^2, \tag{19}$$

where k_s is the rate constant, a_v is the specific surface area for precipitate growth related to the local precipitation faction and DS is the saturation degree. Moreover, $\gamma_{Ca^{2+}}$ and $\gamma_{SO_4^{2-}}$ represent the ionic activity coefficients calculated from the Pitzer model (Sheikholeslami and Ong, 2003). K_{sp} is the thermodynamic solubility product, and a_{H_2O} is the activity of water. C_{salt} is the solute concentration, and calcium sulfate, the most commonly investigated inorganic salt, is associated with gypsum scaling.

Nucleation within liquids requires a higher supersaturation degree and nucleation of particles; thus, only surface nucleation in the supersaturated region is considered (Dydo et al., 2004). New nuclei with a constant diameter appear only in areas without existing crystals, and their nucleation rate is governed by the probability P_N^0 $(0 < P_N^0 < 1)$, which represents the number of nuclei formed per unit time $\Delta\tau$ per elemental surface ΔA (Radu et al., 2014a; Uppu et al., 2020). In the supersaturated region, the outer nuclei, i.e., particles within 2 discrete grid distances from the particle–fluid interface, expand by absorbing nearby solutes, which manifests as an increase in mass m_p. As the particles grow, particle splitting occurs when the diameter calculated under the assumption of constant density reaches a critical value. The inner dense layer ($\varepsilon_c < 0.01$), i.e., particles spaced at a distance from the interface of more than 2 discrete grids, is not involved in growth or salt consumption (Radu et al., 2014a).

$$P_N^0 = \frac{dm_0}{dt} \Delta A \Delta \tau, \tag{20}$$

$$\frac{dm_p}{dt} = k_s A_c \left(\sqrt{DS} - 1\right)^2, \tag{21}$$

where A_c is the mean contact area.

In each simulation loop, the following steps are executed sequentially, as described in Fig. 2: (1) Pre-CFD simulation and saturation detection based on the concentration field; (2) surface nucleation and deposited particle growth in the supersaturation zone; (3) redivision of the CFD mesh and post-CFD simulation.

Uppu et al. (2020) and Prakash et al. (2023) simplified the above approach by not dividing the particle deposition domain and denoted the effect of scaling on permeation and flow by the deposited layer resistance R_f and source term S_{m3}.

$$\frac{dm_0}{dt} = A_N e^{\frac{a_N}{\ln^2(DS)}}, \tag{22}$$

$$\frac{dm_1}{dt} = 3^{\frac{2}{3}} (2\pi)^{\frac{1}{3}} k_R V_m \left(\sqrt{DS} - 1\right)^2 m_0 \left(\frac{m_1}{m_0}\right)^{\frac{2}{3}} + \frac{\pi}{12} \left(\frac{2\sigma V_m}{k_R N_A T \ln(DS)}\right)^3 A_N e^{-\frac{a_N}{\ln^2(DS)}}, \tag{23}$$

$$R_f = \frac{\phi}{1-\phi} R_m, \tag{24}$$

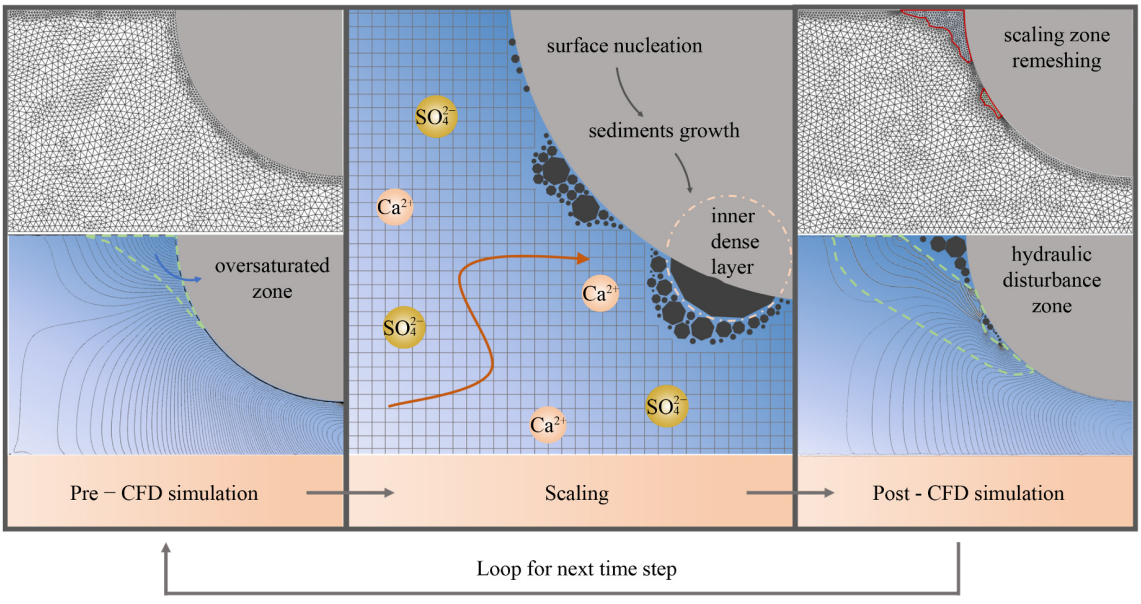

Fig. 2 Schematic of the numerical implementation method of scaling model.

$$\phi = (\pi m_0)^{\frac{1}{3}}(12m_1)^{\frac{2}{3}}/4, \tag{25}$$

$$S_{m3} = \frac{\partial m_1}{V_m N_A \partial t \partial z}, \tag{26}$$

where A_N, a_N and k_R represent the rate parameters. m_0 and m_1 represent the number and volume of deposits on the unit surface, respectively. V_m is the molar volume of the deposit particle, η_{cr} is the critical volume of the nuclei, N_A is the Avogadro number, T is the temperature, σ is the surface energy for hydrogenous nucleation and ϕ is the fractional membrane surface coverage.

Radu et al. (2014a) directly applied the Brinkman flow (Brinkman, 1949) considering the viscous effect and pressure gradient in the sediment domain with the porous media assumption:

$$\frac{\mu}{\kappa}\overrightarrow{v} + \nabla p = \frac{\mu}{\varepsilon}\nabla^2\overrightarrow{v} - \frac{1}{\varepsilon}\left(\frac{2}{3}\mu - \kappa\right)\left(\nabla\cdot\overrightarrow{v}\right), \tag{27}$$

where κ is the hydraulic permeability and ε is the porosity. The second term on the right side of the equal sign can be omitted.

The scaling model described above is computationally intensive due to the monitoring of each deposited particle and mesh redivision in each calculation loop. Mao et al. (2021) monitored the fouling trends of gypsum in full-scale brackish water reverse osmosis (RO) modules using the Scaling Index (SI), which essentially utilizes the concentration as a monitoring indicator:

$$\mathrm{SI} = \log(C_{Ca^{2+}} C_{SO_4^{2-}}/K_{sp}), \tag{28}$$

4.2 Biofouling

4.2.1 Discrete cellular automata (CA) biofilm model

In 2009, a research team led by Picioreanu et al. (1998a; 1998b; 2001) proposed a sophisticated 3D computational model coupling biofouling based on the cellular automata method and CFD. The numerical implementation of the biofilm model can be divided into attachment, growth and multiplication and detachment processes, which are consistent with the growth processes of microbial communities.

The CA model also adopts the strategy of dual parallel meshes in the scaling model mentioned in Section 4.1 by replacing the sediment particle mesh with a biomass mesh. The biomass matrix in CFD is numerically constructed by setting the material properties such that the matrix has a high viscosity. The microbes are attached randomly on the solid surface with a constant biomass attachment rate. Picioreanu et al. (2009) set a maximum shear stress for the surfaces of the biomass to be adsorbed. Microbial proliferation is controlled by the growth rate of biomass, r_X, as described in detail in Section 4.2.2. Once the biomass concentration in one cell exceeds the predefined value $C_{X,M}$, the saturated cell divides into adjacent cells. Randomly redistributed biomass (i.e., 40%–60% (Picioreanu et al., 2004) or 45%–55% (Radu et al., 2015)) is preferred to avoid subsequent synchronous splitting. Radu et al. described and simulated the detachment, erosion and collapse of biomass (Radu et al., 2010). The biofilm parameters can be found in Table 4. In this method, the biomass is removed if the local von Mises stress σ exceeds the biomass mechanical strength σ_{det}, which remains constant as a material property. Furthermore, a straightforward approach of setting a maximum biofouling layer thickness (500μm) (Picioreanu et al., 2004) or a maximum biomass concentration $C_{X,m}$ ($8000\mathrm{mol-C/m^3}$) (Radu et al., 2012) is used.

In each simulation loop, the following steps are executed sequentially, as described in Fig. 3: (i) biomass adsorption; (ii) biomass multiplication and expansion; (iii) biomass boundary determination and CFD remeshing; (iv) CFD calculation; (v) biomass desorption. The fluid flow and substrate concentration are treated as stationary during the biomass calculation time step (several hours) compared to the short CFD calculation time step (several seconds). As foulant accumulates, biomass gradually cover membrane and spacer surfaces

Table 4 Parameters of the in biofilm model

Meaning	Attachment rate, r_{att}	Yield coefficient, Y_{SX}	Maximum specific rate, μ_{max}	Half-saturation coefficient, K_S	Maximum Biomass concentration, $C_{X,M}$	Biomass mechanical strength, σ_{det}	Diffusion coefficient for substrate, D_{sub}
	Cmol/(m^2·d)	molC/molbiomass	d^{-1}	mol/m^3	Cmol/m^3	N/m^{-2}	m^2/s
Picioreanu et al. (2009)	6×10^{-4}	0.52	2.8	0.063	2800	–	2.5×10^{-9}
Radu et al. (2010)	5×10^{-3}	0.5i	2	0.025	8000	7	10^{-9}
Radu et al. (2012)	$5\times10^{-3}, 15\times10^{-3}$	0.5	2	0.025	8000	7	10^{-9}
Bucs et al., (2014a)	0.06, 0.13, 0.26	1	1.08	0.05	1400	–	10^{-9}>
Radu et al. (2015)	5×10^{-3}(C – mol/(m • d)	0.5i	2	0.025	`	7	10^{-9}

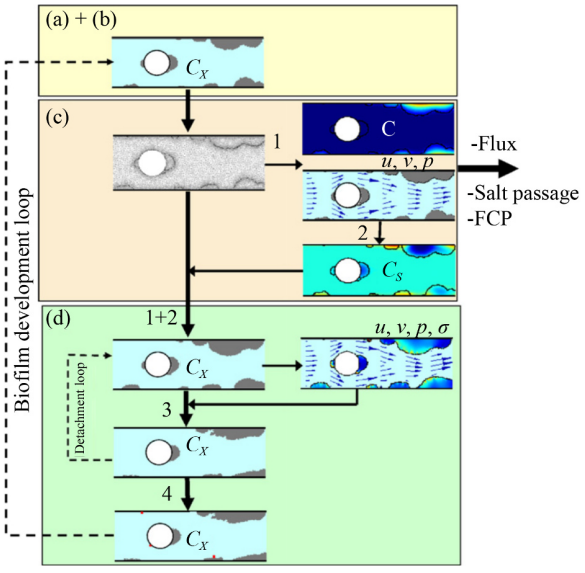

Fig. 3 Schematic of the numerical implementation method of the biofouling model (Radu et al., 2010).

and significantly alter the hydrodynamics and permeate performance, which serve as the key metrics for researchers.

The biomass growth rate, r_X, is controlled by the local substrate concentration. One limiting compound concentration C_s is adopted and governed by the mass balance equation in Eq. (3) considering Monad kinetics (Monod, 1941):

$$S_{m3} = r_S = Y_{SX} r_X, \tag{29}$$

$$r_X = \mu_{\max} \frac{C_s}{(K_S + C_s)} C_X, \tag{30}$$

where r_S is the substrate consumption rate in the biomass subdomain, r_X is the biomass growth rate, Y_{SX} is the yield, $\mu_{\max}$ is the maximum specific growth rate, K_S is the half-saturation coefficient and C_X is the biomass concentration. The diffusion coefficient D for the substrate in Eq. (3) in the biofilm region can either be set as that in the fluid domain D_w or adjusted via the porosity ε_c (Bucs et al., 2016):

$$D = \varepsilon_c D_w. \tag{31}$$

As confirmed by Vrouwenvelder et al. (2009c), diffusive flux is substantially greater than convective flux when considering the mass transfer of the substrate near the membrane, which may help demonstrate that the presence or absence of flow within the biomass has little effect on the accuracy of the overall calculation. The biomass region is considered to be impermeable due to its low permeability, which is on the order of 10^{-16} m^2/s (Fowler and Robertson, 1991; McDonogh et al., 1994). Therefore, under this assumption, the substrate is controlled by convection and diffusion in the fluid domain, while diffusion occurs only within the biomass domain (Bucs et al., 2014a).

However, understanding the flow and mass transfer within biomass is crucial once large areas of biofouling result in severe dead zones, solute accumulation and permeation blocks. Although poor mass transfer can reduce substrate concentrations in biomass regions, subsequent poor hydrodynamic conditions (e.g., low velocity and shear stress) have complex and multifaceted effects on biomass growth. Importantly, shear stress has a dual influence on membrane fouling. On the one hand, a high shear stress promotes mass transfer to mitigate substrate accumulation near the membrane (Schwinge et al., 2002a; Koutsou and Karabelas, 2015) and promotes scouring and destruction of existing biomass (Koutsou and Karabelas, 2015). On the other hand, high steady shear stress may cause microbial attachment (seeding), consequently leading to the early development of biofouling (Radu et al., 2010; Lecuyer et al., 2011; Wang et al., 2013; Saur et al., 2017). Additionally, fluctuating unsteady shear stress can help minimize biofilm attachment (Kerdi et al., 2018). The Brinkman flow mentioned in Section 4.1 can be employed in biomass layers with constant thicknesses (Jeong et al., 2020), as well as in regions occupied by the microbial cells, as described in Section 4.2.1.

Despite its simplicity, this solution has several shortcomings: (i) Detached biomass, ranging from single-celled microorganisms to small biomass residues to large microbial colonies, is immediately removed from the system. This assumption does economize calculation resources. However, this approach ignores the clogging by dislodged biomass debris, which can commonly occur in the narrow flow channel of the membrane module; (ii) the assumption of a constant mechanical strength σ_{det} may not accurately represent the varied mechanical properties of different types and growth stages of microorganisms; and (iii) natural decay processes are not accounted for.

4.2.2 Simplified approach: biofouling resistance and artificially established biomass geometry

Systematic modeling of the biofilm development process is consistent with the real situation, but it is preferable for studies that are concerned only with the effect of biomass on flow and permeation to disregard the individual microorganisms and adopt a simplified approach.

Mohan et al. considered the combined EPS and SMP (CES) model (Janus, 2014; Janus and Ulanicki, 2015) to be more reliable than the sectional resistance model (Li and Wang, 2006) and adopted the former model to simulate biofouling in MBR. The CES model, which assumes that soluble microbial products (SMPs) cause irreversible fouling and that extracellular polymeric substances (EPSs) cause reversible fouling, is embedded in the fouling resistance R_f in Eq. (4) (Mohan et al., 2022):

$$R_f = R_i + R_r, \tag{32}$$

$$R_i = a_i k_i e^{b_i J} J \times C_{SMP}, \tag{33}$$

$$R_r = \left(1.376 \times 10^{12} \frac{C_{EPS}}{C_{MLVSS}} - 2.564 \times 10^{13}\right) \times (C_{MLSS} \times J - m_{r,back}), \tag{34}$$

where R_i and R_r are the resistances of irreversible fouling and reversible fouling, respectively. a_i, b_i, and k_i are coefficients, and C_{EPS}, C_{MLSS}, C_{SMP}, and C_{MLVSS} are the concentrations of each component. $m_{r,back}$ represents the detached fouling cake due to backflow.

Treating microorganisms as solid domains to study surrounding fluid dynamics is another approach. Petrosino et al. used spherical particles to determine that bovine serum albumin (BSA) causes fouling during ultrafiltration. Three regions with different protein concentrations are selected corresponding to different particle volume fractions within the Monte Carlo box as shown in Fig. 4(a). CFD simulations are performed in the fluidic domain after removing the particle domain, and the calculated impedance of the protein-contaminated layer shows an uncertainty of only 4% from the experimental validation (Petrosino et al., 2023). Luo et al. (2022) conducted CFD simulations with staggered impermeable cylinders representing the cells and a loose EPS layer covering the membrane surface as shown in Fig. 4(b); these researchers reported that a high EPS concentration significantly increased the pressure drop and filtration resistance of the biofilm. Lin et al. (2023) manually established a biomass regularly distributed on filaments as shown in Fig. 4(c) to represent the effect of biofouling on the hydrodynamic characteristics of flow channels.

4.3 Colloidal particles

4.3.1 Porous cake layer

As colloidal particles accumulate, the membrane surface is covered with a porous cake layer ranging from one to one hundred micrometers in height. According to the cake-enhanced osmotic pressure (CEOP) theory (Chong et al., 2008; Fimbres Weihs and Wiley, 2014), the porous cake hinders solute back-diffusion and increases the concentration polarization and osmotic pressure, thus significantly reducing the near-membrane mass transfer and permeation flux.

The hindering effect on flow within the porous layer caused by the fouling layer is expressed using the momentum source term $\boldsymbol{S}_{m2}$ in Eq. (2) (Zhuang et al., 2018). The cake layer impedes solute diffusion within the porous domain, which is achieved in numerical simulation by strengthening the diffusion coefficient D_{sc} based on the solute diffusion coefficient without the cake layer D_s (Boudreau, 1996).

$$\boldsymbol{S}_{m2} = -\varepsilon_c \mu (R_m + R_c) \boldsymbol{v} / \delta, \tag{35}$$

$$D_{sc} = \frac{\varepsilon_c}{1 - \ln \varepsilon_c^2} D_s, \tag{36}$$

where ε_c is the porous domain porosity, δ is the porous layer height and R_c is the resistance caused by the fouling layer.

The additional cake layer resistance R_c, representing the hindering effect of particle accumulation on the membrane surface, is introduced into Eq. (4). The following is

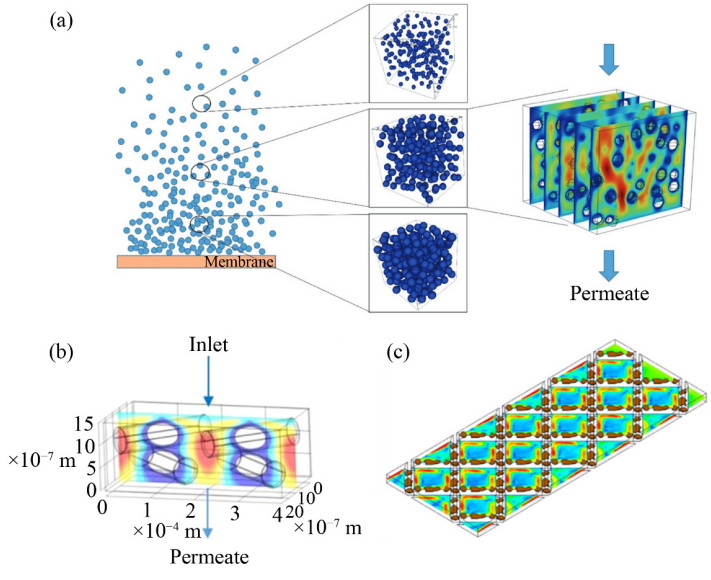

Fig. 4 Schematic of the artificially established biomass geometry: (a) various concentration of BSA particles in the Monte Carlo box (Petrosino et al., 2023); (b) cylinders represent the EPS layer covering the membrane surface (Luo et al., 2022); and (c) the manually established biomass domain is regularly distributed on filaments (Lin et al., 2023).

the general form of the cake layer resistance:

$$dm_c/dt = S_c, \tag{37}$$

$$dR_c/dt = \alpha dm_c/dt = \alpha S_c, \tag{38}$$

where m_c is the local cake layer mass determined by the particle deposition rate and α is derived from the cake layer porosity ε_c, particle diameter ε_c and particle density ρ_c based on the Carman–Kozany equation ($\alpha = \frac{180(1-\varepsilon_c)}{\rho_p d_c^2 \varepsilon_c^3}$) (Carman, 1997). According to critical flux theory, S_c is determined by the net flux ($J - J_{crit}$), the particle deposition ratio θ, and the local particle concentration C_p as follows.

$$S_c = \theta C_p (J - J_{crit}). \tag{39}$$

In cross-flow filtration, θ depends on the local shear rate (Knutsen and Davis, 2006), which ranges from 0–1. The critical flux J_{crit} is influenced by Brownian diffusion and shear-induced diffusion, which results from the low Reynolds number in the filtration system and the typical size of colloidal particles. The detailed calculation methods for θ and J_{crit} are described in the Supplementary Material.

Considering the effect of solute concentration on porosity, Fimbres Weihs and Wiley (2014) proposed a new calculation method for α using the Carman–Kozany equation as a basis:

$$\alpha = \frac{180\xi'}{\rho_p d_c^2 \xi''}, \tag{40}$$

$$\xi' = \int_{\varepsilon_{c,w}}^{\varepsilon_{c,c}} \frac{(1-\varepsilon_c)(2\varepsilon_c - 3)}{\varepsilon_c^3 \{1 - 0.026\left[\frac{\varepsilon_c^3(1-\varepsilon_{c,w})}{\varepsilon_{c,w}^3(1-\varepsilon_c)}\right]^{2.955}\}} d\varepsilon_c, \tag{41}$$

$$\xi'' = \int_{\varepsilon_{c,w}}^{\varepsilon_{c,c}} \frac{(2\varepsilon_c - 3)}{1 - 0.026\left[\frac{\varepsilon_c^3(1-\varepsilon_{c,w})}{\varepsilon_{c,w}^3(1-\varepsilon_c)}\right]^{2.955}} d\varepsilon_c, \tag{42}$$

where $\varepsilon_{c,c}$ and $\varepsilon_{c,w}$ represent the porosity at the cake–fluid interphase and at the cake–membrane interphase, respectively.

A similar form of bovine serum albumin (BSA) was used for membrane fouling (Schausberger et al., 2009):

$$\alpha = \left(\frac{\Delta P}{\mu J^{1h}} - R_m\right)/\dot{m}_c^{1h}, \tag{43}$$

$$S_c = A(C_p)^{0.6}(\dot{m}_c^{eq} - \dot{m}_c), \tag{44}$$

where $\dot{m}_c$ is the amount of substance per membrane of deposited BSA. The superscript eq indicates equilibrium deposition, while $1h$ indicates one hour of filtration.

Su et al. (2019) gradually increased the porosity of the porous medium ε_c in the porous cell on the membrane surface via particle deposition. The porous cell is treated as a "fully deposited cake cell" as ε_c reaches the critical value of 0.4, after which the process of particle deposition and increasing porosity is transferred to the upper cell. AlthoughUppu et al. (2019) stated that ε_c is related to solute concentration C_s, these researchers still used the assumption of constant cake layer porosity because the concentration boundary layer is much larger than the thickness of the cake layer:

$$\varepsilon_c = 0.209 - 0.0417 \lg C_s. \tag{45}$$

Several methods subtly differ from the above formulas for calculating the cake layer resistance R_c and thickness h_c. In general, these methods are all controlled by the flux J and the near-membrane concentration.

Movahedi and Jamshidi (2022) adopted integral equations based on $dR_c/dt = kC_pJ$ for the simulation of colloidal clay:

$$R_c + R_m = (R_{c0} + R_m) \times \left(1 + \frac{2k\Delta P C_p t}{\mu(R_{c0} + R_m)^2}\right)^{\frac{1}{2}}, \tag{46}$$

$$h_c = \int_0^t J C_p C_{EX} dt, \tag{47}$$

where R_{c0} is the resistance of the first cake layer deposited over the membrane surface, k is a constant parameter, ΔP is the pressure difference through the membrane, μ is the fluid viscosity and t is the filtration time. C_{EX} represents the expansion of the cake layer due to interparticle water, swelling, compaction and particle settling and is determined by experimental measurements.

Al-Abbasi and Bin Shams divided the silica gel layer into a gel layer and an adsorption layer:

$$R_c = R_g + R_a, \tag{48}$$

$$dR_g/dt = k_g J^* \left(\frac{\Delta P}{\mu J^*} - R_g\right), \tag{49}$$

$$R_a = k_a C_p, \tag{50}$$

$$h_c = \int_0^t J \hat{C}_p dt, \tag{51}$$

where R_g is the gel layer resistance, R_a is the adsorption layer resistance, k_g and k_a are coefficients, J^* is the critical flux, C_p is the silica gel concentration on the membrane surface and $\hat{C}_p$ is the silica gel volume fraction on the membrane wall (Al-Abbasi and Bin Shams, 2021).

Rajabzadeh et al. (2010) reported that membrane fouling caused by soy protein extracts involves both reversible R_r and irreversible R_i fouling resistance. This reversible fouling is predominantly attributed to CP, and irreversible fouling is attributed to protein adsorption at membranes via first-order kinetics:

$$dR_i/dt = C_p(\alpha - R_i)/k, \tag{52}$$

$$R_r = \beta(1 + \lambda \Delta P), \tag{53}$$

where the parameters α, β, λ, and k are determined by experiments.

4.3.2 Particle trajectory

Targeting the resistance of porous regions on membranes may not satisfy the accuracy requirements of some studies, such as those on the deposition process of the cake layer, the movement of particles through the micropores in the membrane, and interactions between particles and particles and between particles and the membrane. An alternative approach is needed to track the trajectory of the particles. The widely adopted Lagrangian approach is as follows:

$$m_p \frac{\partial^2 \vec{r}}{\partial t^2} = \vec{F}, \tag{54}$$

where $\vec{r}$ is the particle position, m_p is the particle mass and $\vec{F}$ is the net resultant force, consisting of the fluid-induced force (drag force, lift force) (Shang et al., 2022b; Zhang et al., 2022), contact force in collision (Lohaus et al., 2018), body force (gravitational force, buoyancy force, electric force), added mass force, near-surface force described in XDLVO theory and Brownian random force (Jung and Ahn, 2019). Because the simulation systems in most studies involve dilute solutions (<10% v/v), the reaction force of the particles on the fluid is negligible (Rahimi et al., 2009). Using a built-in module in CFD software, such as the discrete phase model (DPM), the particle transport task considering force balance can be achieved (Rahimi et al., 2009).

Interestingly, the particle tracking approach can be coupled with the resistance of porous media approach. Jung and Ahn (2019) linearly transferred the thickness of the deposited particle h_c to the cake layer resistance R_c:

$$R_c = h_c \alpha \rho_p (1 - \varepsilon_c), \tag{55}$$

where α is defined in Eq. (38), ε_c is the porosity of the cake layer, which is assumed to be 0.4, and ρ_p is the density of the particle.

Radu et al. (2014b) disregarded the resultant forces on the particles to avoid complicated mechanical calculations and treated the local fluid velocity as the particle velocity in the deposition process of microspheres mimicking bacterial cells on the SWM surface. Once the wall adhesion condition is met, i.e., when the particle–wall distance drops below 5 μm and the particle velocity fails below 1 μm/s, the particle is removed from the simulation domain, and the deposition location is simultaneously recorded. Similarly, Ma et al. (2019) used the Eulerian–Eulerian multiphase model to simulate the sludge distribution in a hollow-fiber MBR, where the behavior of the sludge deposition is controlled by the probability ∅:

$$\varnothing = \frac{24J}{24J + C_d d_p G}, \tag{56}$$

where C_d is the coefficient of the drag and lifting force, d_p is the diameter of the sludge particle and G is the velocity gradient. The Eulerian–Eulerian multiphase model has also been applied as an approach for observing particle distributions (Fang and Wu, 2008; Wu and Lin, 2012).

Collision detection and contact force calculations are critical for tracking the motion of massive amounts of particles deposited on a membrane surface. The built-in multiphase and discrete phase model in conventional CFD software (ANSYS-Fluent®, OpenFOAM®, COMSOL®) is not capable of handling these calculations; thus, the discrete element method (DEM) is needed to assist in the particle calculation, i.e., CFD–DEM coupling. The open-source software CFDEM®, which combines fluid (OpenFOAM®) and particle (LIGGGHTS®) calculations, is widely utilized (Lohaus et al., 2018; Li et al., 2019; Puderbach et al., 2021; Bräsel et al., 2023). Lohaus et al. (2018) reported that the interaction between particles and the inner structure of membrane pores critically affects pore clogging. In particular, particle re-entrainment in the pore channel and reattachment lead to severe fouling or even complete blockage. Bräsel et al. (2023) identified a correlation between cake layer morphology and filtration conditions. A higher cross-flow velocity leads to a denser cake layer, and a lower velocity leads to more particle deposition and a greater flux decline. Moreover, an increase in transmembrane pressure exacerbates pore clogging. Li et al. (2019) investigated the effects of the particle size distribution, liquid viscosity and compressibility of the cake layer on the filtration performance.

4.4 Issues for a more realistic model

4.4.1 Combined fouling model

It has been fairly well documented that fouling in pressure-driven membrane modules tends to manifest as multiple concomitant types. Thompson et al. (2012) identified gypsum crystals within the biomass matrix on RO membranes and illustrated that the biofilm substantially augmented mineral fouling.

Zhang and Klapper (2010) developed a combined model of biofilm-induced calcite precipitation using the Euler-Euler approach, which is limited in addressing interphase surface interactions like sediment surface nucleation and biofilm encapsulation behavior. Notably, the biomass in this study catalyzed urea degradation, consequently generating precursor inorganic salts for the scaling process.

Olivera-Nappa et al. (2010) developed a two-dimensional model that integrates both biomass and inorganic sediments to investigate the biochemical processes of biofilm development and metal element leaching on mineral ore surfaces. In the premise of particle-represented biomass versus sediment, the following synergies exist between biomass and sediments: (i) Biomass utilizes inorganic sediments as a substrate, (ii) The diffusion coefficients of inorganic salts are affected by particle

concentration, and (iii) Sediments are exclusively generated on the outer surface of the bioparticle. The model developed by Radu et al. in 2015, considering calcium sulfate scaling and biofouling, stands as the most comprehensive and intensive simulation study on combined fouling in pressure-driven membrane systems to date (Radu et al., 2015).

However, current numerical modeling studies on combined fouling have limitations. Most studies focus on the synergistic effects between mineral scaling and biofouling, while neglecting the effects of organic foulants and colloidal particles in combined fouling. A synergistic effect has been observed between organic fouling and scaling in forward osmosis systems. The early conditioning layer formed by organics on the membrane surface may inhibit the nucleation and development of gypsum crystals, while alginate-based organics can interact with calcium ions, thereby promoting scaling (Chun et al., 2020). No simulation studies have been conducted to model combined fouling incorporating these mechanisms.

4.4.2 Large-scale & full-scale simulation

As shown in Table 1, the simulation domain in most studies is limited to several cells divided by spacers, assuming periodic boundary conditions. While this approach is sensible for avoiding redundant calculations and conserving computational resources, it may not accurately represent the non-periodic nature of the filtration vessel, particularly for the lead and tail elements in full-scale systems, where the bulk flow concentration increases as permeation proceeds (Thompson et al., 2012; Gorzalski and Coronell, 2014). This highlights the significance of conducting simulations on large-scale membrane modules and even full-scale plants comprising multiple filtration elements.

Li and Tung (2008) demonstrated the critical role of computational domain size in accuracy by comparing simulated pressure drop values with experimental data. An optimal scale of 18 × 8 cells was determined for its lowest pressure drop deviation (~7%). With advancements in computer performance, larger-scale simulations have become feasible. Wei et al. (2021) conducted a large-scale three-dimensional CFD simulation on spiral wound RO membrane module with dimensions of 2.05 m length, 0.9 m width, an effective membrane area of 400 ft^2 and approximately 13 million mesh elements. Sitaraman and Battiato (2022) simulated a two-dimensional axisymmetric RO membrane with a length of 1m and approximately 14 million mesh elements.

Large-scale simulation is not just a simple zoom of the small-scale simulation under the assumption of periodicity, but more importantly it furnishes the spatially and temporally varying hydrodynamic parameters for individual filtration element and assists in identifying potential fouling regions under actual operating conditions. The mass transfer correlations, typically in the dimensionless power-law form of $Sh = \alpha Re^{\beta} Sc^{\gamma}$ (constants α,β, and γ are determined based on geometry and system type), can be derived from parameter fitting through large-scale simulations. According to the mass transfer coefficient data, the one-dimensional model in full-scale system of solute concentration, concentration polarization modulus, solute flux, water flux and pressure loss as a function of length/element stage can be obtained (Guillen and Hoek, 2009; Gu et al., 2021). Chong et al. (2022) adapted the aforementioned calculation method by conducting CFD simulations with dissolving-impermeable membrane. They then applied the obtained mass transfer correlations to calculate the permeate parameters of a full-size system with permeable membrane, which is valid as long as the ratio of volumetric flow rate to mass transfer coefficient is less than 20. Liang et al. (2019) extended their work by developing a techno-economic model to evaluate the water production performance, mass transfer effect and economic cost of different spacer geometries.

A more direct approach for full-scale simulation is transferring the outlet boundary conditions of the previous element to the inlet boundary conditions of the next element for sequential calculation (Keucken et al., 2018). Alternatively, merging multiple elements by disregarding the connecting pipes and valves is proposed (Mao et al., 2021), However, this method is evidently not cost-effective for dealing with complex geometries and multistage systems.

4.4.3 Validation

Experiment validation serves as a direct approach to verify the accuracy of pressure-driven membrane fouling models. Apparent hydrodynamic parameters obtained from experiments, such as pressure drop (Akagi et al., 2018; Gu et al., 2021; Kerdi et al., 2021; Guan et al., 2023), velocity distribution (Qamar et al., 2019), permeate flux (Gu et al., 2021), shear stress (Kavianipour et al., 2017), friction coefficient (Liang et al., 2019), CP modulus (Gu et al., 2021; Sitaraman and Battiato, 2022), and ATP/TOC concentration of attached biomass (Lin et al., 2020), are commonly used as validation metrics. Qualitative comparison of flow characteristics and hydrodynamic trends with literatures can also aid in simulation validation (Chong et al., 2022). Achieving exact consistency between experimental and simulated geometries is challenging in simulation studies aimed at optimizing spacer geometry. Hence, comparisons of dimensionless correlations among similar structures, such as dependence of Sh on Pn (Sutariya et al., 2022; Chong et al., 2023), dependence of Sh on Re and Sc (Liang et al., 2019; Sitaraman and Battiato, 2022), and dependence of friction coefficient f on Re (Mokhtar

et al., 2021), serve as reasonable alternatives. Cao et al. (2018) utilized polystyrene beads to replace microbial cells in filtration experiments, validating the accuracy of the proposed microbial deposition-adhesion model.

Although experimental apparent parameters reflect the macroscopic influence of membrane fouling and provide strong corroboration for the accuracy of the CFD simulation and fouling model, microscopic characterization technique is required to determine the morphology and distribution of foulants on the membrane. This is critical for investigating the development of complex biofouling/scaling. *In-situ* Optical Coherence Tomography (OCT) is employed to capture images on spacer filaments and membrane surfaces, confirming the good agreement between experimental biomass distribution and the hydrodynamics obtained from simulation work (Ali et al., 2019; Kerdi et al., 2020; 2021). Picioreanu et al. obtained biofilm morphology by OCT to investigate its elastic-viscous properties, which provided crucial data for the biofouling model (Jafari et al., 2018; Picioreanu et al., 2018). Confocal laser scanning microscope (CLSM) with fluorescence dyeing enables mapping of biomass distribution on a broader range of membrane surfaces, validating its agreement with CFD results (Lin et al., 2022b; 2023). Besides foulant distribution, changes in flow patterns within membrane modules altered by membrane fouling have received considerable attention, necessitating non-invasive real-time observation techniques. Doppler OCT provides a method to visualize the velocity distribution in a two-dimensional plane within the flow channel, enabling accurate validation of CFD results (Gao et al., 2013; Park et al., 2016). Overall, the current experimental work has adequately confirmed the reliability of CFD simulations coupled with fouling models.

5 Numerical construction of the antifouling strategy

5.1 Patterned membrane

The use of micropatterned membranes is considered an effective method for mitigating membrane surface fouling. Typical patterns as shown in Figs. 5(c)－5(h) include waves (Zhao et al., 2020), rectangles (Shang et al., 2020a), prisms (Lee et al., 2013), pyramids (Choi et al., 2015), trapezoids (Won et al., 2016), and arches (Shang et al., 2021). The generally studied pattern sizes are at the micrometer or millimeter level, while nanoscale patterns do not contribute to membrane fouling mitigation (Shang et al., 2020b).

Cross-flow filtration creates vortices in the valleys of the patterned membrane that grow with increasing cross-flow velocity, which enhances localized mass transfer and disturbs the boundary layer, thus leading to better performance than that yielded by the flat membrane. Ilyas et al. (2022) observed vortex formation and convection away from the valley in vibrating patterned membranes, which significantly reduced the fouling rate compared to flat membranes. Shang et al. (2021) reported that arch and trapezoidal patterns substantially increase the mass transfer coefficient (> 3 times that of a flat membrane) and decrease the CP factor (< 60% of a flat membrane).

The streamlines (Fig. 5 (a)) obtained by Choi et al. (2015) further revealed that the vortex stream inside the valley and the main flow stream are separated from each other, which makes it difficult for particles to enter the valley. Due to flow scouring, particles are deposited primarily at the surface in the mainstream direction rather than facing the mainstream. An increase in the permeate flux is accompanied by an increase in the vortex streamline toward the bottom, which indicates that the region of potential particle deposition moves from the upper part of the valley down to the bottom. Contrary to common sense, a higher cross-flow velocity leads to a higher collision frequency, which may lead to more severe particle deposition (Choi et al., 2015). However, the opposite conclusion was drawn by additional studies. Won et al. (2016) concluded that a higher cross-flow velocity triggers greater shear stress near the pattern and vortices closer to the main flow, which facilitates the reentry of particles in the valley and thus alleviates particle deposition. Jung and Ahn (2019) suggested that particles barely touch most of the surface in a valley at high cross-flow velocities, which indicates stronger particle remixing to the bulk flow and less membrane fouling. In their study, they also determined that depositing large particles on patterned membranes is difficult as shown in Fig. 5 (b). By analyzing particle trajectories, Shang et al. (2022b) also supported the viewpoint that a high cross-flow velocity reduces membrane fouling.

Despite the above advantages of patterned membranes, Shang et al. (2022a) cautioned about their higher CP factor, which results in more severe fouling of inorganic salts and organic small molecules. This tendency is worsened by improper orientation of the pattern, especially when the pattern is perpendicular to the flow. Although the patterned membrane enhances the shear stress in the upper part of the valley, this stress is reduced in the whole domain, especially at the valley bottom (Lee et al., 2013).

Changes in the patterned morphology affect the microscopic flow field, which in turn yields different permeate performances and antifouling capabilities. Shang et al. (2020a) noted that conventional membranes with irregular apertures are not effective at resisting fouling. The irregular geometry produces few vortices and has a strong shading effect on foulants entering the valley (Shang et al., 2020a). Won et al. (2016) concluded that trapezoidal patterns have a larger vortex region than

prism patterns, which significantly reduces membrane fouling. Ilyas et al. (2021) conducted CFD simulations of rectangular and trapezoidal patterned membranes of different sizes and noted that trapezoidal patterns and smaller pattern spacings lead to higher velocities in valleys, which is beneficial for reducing foulant deposition. Shang et al. (2021) considered the arch pattern to have a larger high-velocity zone in the valley, stronger reflux velocity, larger membrane area and greater shear stress than the trapezoidal pattern, which proved the potential of the arch shape pattern. Zhou et al. (2021) performed a comprehensive simulation of patterned membranes for shapes including rectangles, trapezoids, prisms, pyramids, cylinders, circles and polyhedrons. Analysis of the flow field confirmed the phenomena of solute accumulation in the valley, high

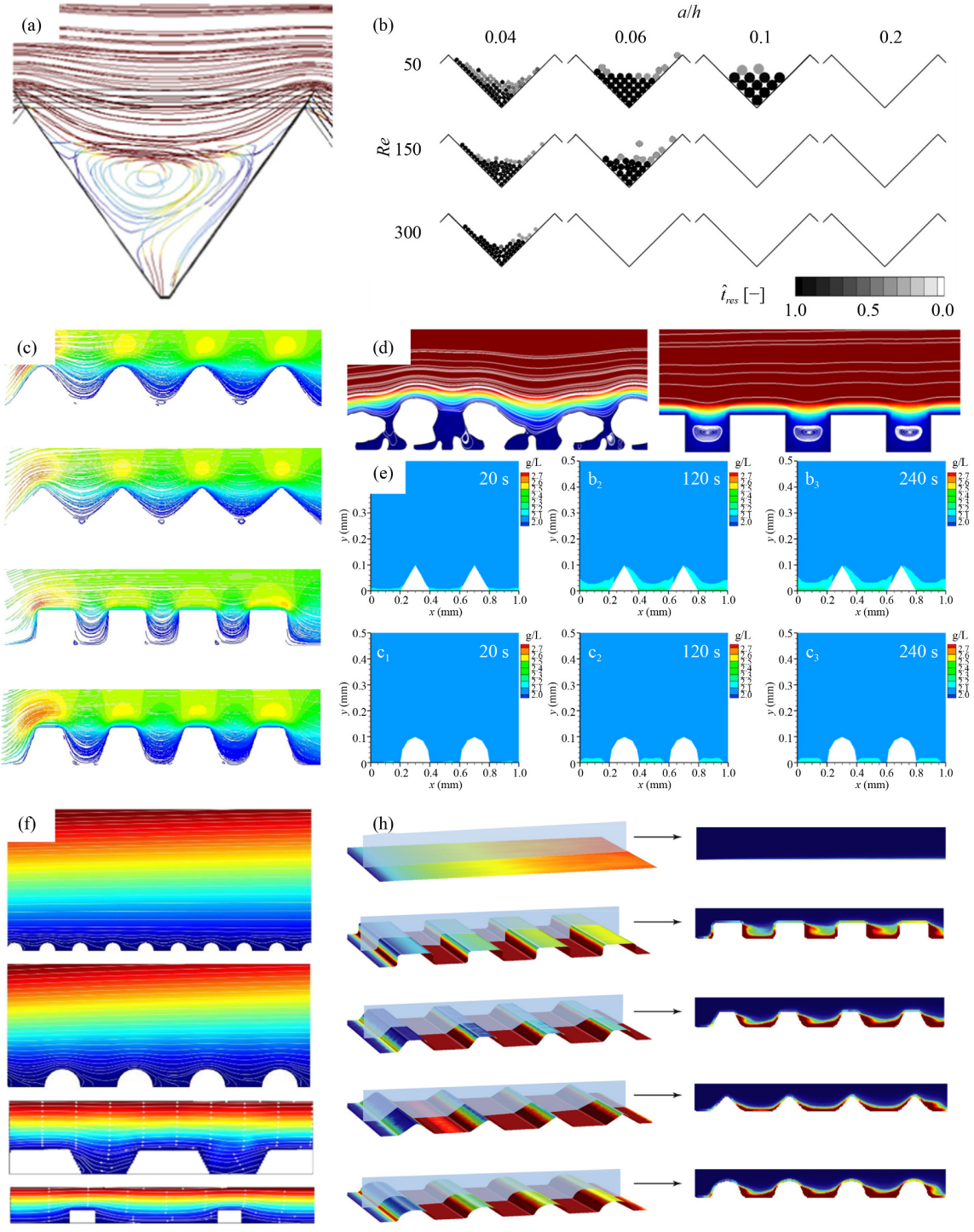

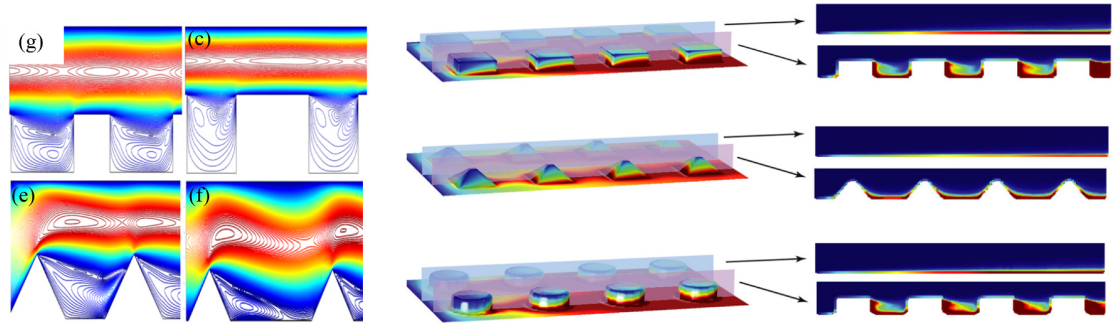

Fig. 5 Simulation results of patterned membranes. (a) stream lines in the valley (Choi et al., 2015); (b) particle distribution on patterned membrane for different particle diameters and Reynolds numbers (Jung and Ahn, 2019); (c) velocity streamline profile for different patterned membranes: wave tri, rec, and trap (Zhao et al., 2021); (d) velocity streamline profile for conventional membrane and rectangular membrane (Shang et al., 2020a); (e) real-time solute concentration distribution for triangular membrane and cambered membrane (Shang et al., 2021); (f) streamlines for different patterned membranes (Shang et al., 2020b); (g) streamlines for rectangular membranes and triangle membranes (Ilyas et al., 2021); and (h) solute concentration distribution for different patterned membranes, namely, rectangles, trapezoids, prisms, pyramids, cylinders, circles, and polyhedrons (Zhou et al., 2021).

shear stress and permeate flux near the peak. More importantly, the additional membrane area of patterned membranes is believed to play a decisive role in counteracting unfavorable hydraulic conditions in the valley area and yielding a higher overall permeate flux than that of flat membranes.

5.2 Vibration

Vibration significantly reduces the probability of foulant deposition on the membrane surface and disrupts the concentration boundary layer.

When the direction of reciprocating vibration is perpendicular to the direction of membrane permeation, the vibration is numerically calculated by setting the periodic velocity $v = 2\pi f A\sin(2\pi f t)$ on the membrane surface (Su et al., 2018), i.e., modifying the source term $\boldsymbol{S}_{m2}$ in Eq. (2):

$$\boldsymbol{S}_{m2} = \begin{cases} \rho(2\pi f)^2 A\cos(2\pi f t)\boldsymbol{i}, \text{on the membrane} \\ 0, \text{in the fluid domain} \end{cases} \quad (57)$$

where i is the normal vector in the vibration direction, f is the vibration frequency, A is the vibration amplitude and t is time.

Ilyas et al. (2022) used a new method of dynamic meshing for the case in which the vibration direction is parallel to the permeation direction. The whole mesh is given a periodic displacement of $A\cos(2\pi f t)$.

Zamani et al. (2013) investigated the effect of vibrating fiber membrane configuration and filament distance on the membrane surface shear rate. There is an optimal fiber distance in the studied configuration (a fiber diameter of 0.8 mm, a vibrating amplitude of 1 cm and a vibrating frequency of 5 Hz), and the staggered configuration produces high maximum wall shear compared to the square-shaped arrangement. Moreover, a larger fiber spacing provides a more uniform shear stress distribution. Su et al. (2018; 2019) compared the performances of various Reynolds numbers, vibration frequencies, vibration amplitudes and vibration times. CP is significantly weakened (up to a 25% reduction in NaCl accumulation, a 60% improvement in the normalized permeate flux and a considerable decrease in deposited particles, as shown in Fig. 6 (a)) by vibration, as evidenced by the increase in the Sherwood number. The antifouling effect increases with increasing vibration frequency and decreases when the *Re* is high; however, it is necessary to consider the balance between the vibration cost and benefit. Interestingly, parameters such as the CP modulus, Sherwood number and permeate flux exhibit sinusoidal variations due to vibration, while no significant changes are found in the flow pattern.

5.3 Rotation

Rotation creates a large shear-enhanced zone on the membrane surface and intensifies mass transfer, which is an effective strategy for mitigating membrane fouling.

The rotating dynamic membrane can be divided into rotating rotors and rotating membranes. The boundary condition with forced velocity in the polar coordinate system is applied on the rotating surface with a constant angular velocity Ω:

$$v_\theta = r\Omega \quad (58)$$

$$v_r = 0 \quad (59)$$

where v_r and v_θ are the axial and tangential velocities, respectively, at a distance of r from the axis.

The rotor, e.g., the impeller or disk, creates a strong swirling flow on the membrane surface. Hwang et al. (2014) reported high shear stress and high velocity (1–2 orders of magnitude greater than the inlet and outlet velocities) on the membrane surface, which led to significant cake layer disruption. Notably, the simulated

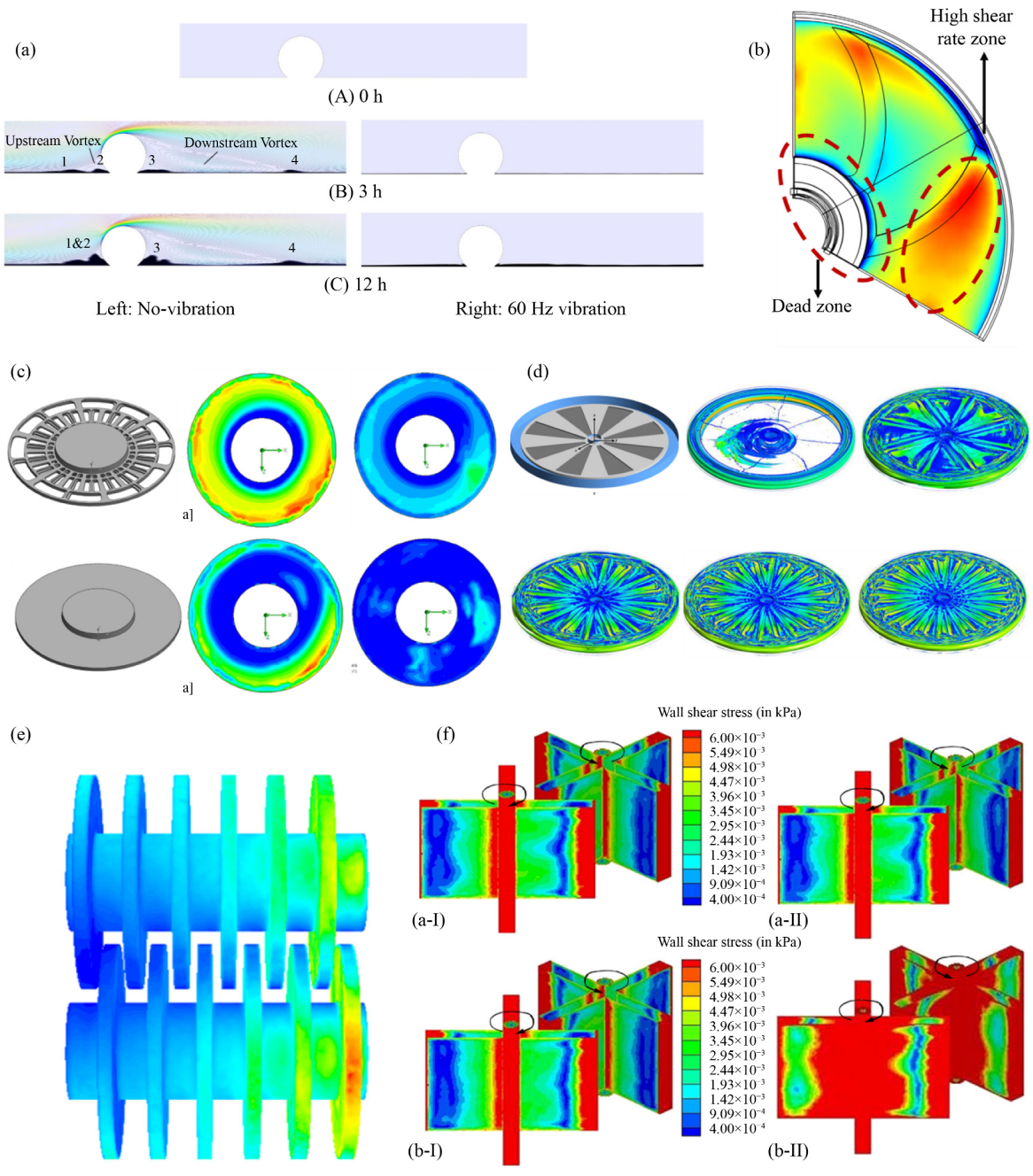

Fig. 6 Simulation results of the vibration and rotation membranes. (a) the deposited particle on no-vibration and 60 Hz vibration membranes (Su et al., 2019); (b) the wall shear stress distribution on the membrane surface with a rotating impeller (Xie et al., 2018); (c) wall shear stress distribution on the perforated and nonperforated disk (Kim et al., 2015); (d) the vortex structures visualized by the λ_2-criterion for etching disks with the number of etching patterns ranging from 0 to 16 (Park et al., 2023); (e) the shear stress distribution on the surfaces of staggered rotating membranes (Zhang et al., 2022); and (f) the shear stress distribution on basket surfaces (Naskar et al., 2019).

shear stress is 15%–50% lower than the shear stress derived from the empirical equations, probably due to the actual filtration geometry. Kim et al. (2015) reported that higher rotational speeds result in more uniform velocities and shear stresses on the membrane surface. The perforated disc performed better than the ordinary disc, as shown in Fig. 6 (c). The average shear stress was well fitted to the flux and fouling layer resistance. Similarly, pattern-etched discs, as shown in Fig. 6 (d), were used to improve the performance of the rotation dynamic filtration system by inducing complex vortexes. The best performance was achieved with a pattern number of 8. However, Park et al. (2023) concluded that the key influencing factor in rotating dynamic membranes is still

the rotational speed. Xie et al. (2018) confirmed that the CFD results aligned well with the PIV data. There is a dead zone near the shaft and a region of high velocity and shear rate at the leading edge of the impeller as shown in Fig. 6 (b), which periodically cleans the outer membrane. Jogdand and Chaudhuri (2015) agreed that there is an annular region with high concentrations and low fluxes near the axis, which poses a high pollution risk, while high feed velocity may weaken the dead region to some extent. Higher rotational speeds and feed pressures correspond to higher permeate fluxes; however, the disadvantage is that the cake layer forms rapidly at high pressure and results in a rapidly decreasing flux (Jogdand and Chaudhuri, 2015; Uppu et al., 2019). The abovementioned team performed a system-level energy analysis and reported that the energy needed to rotate the disk at low rotational speeds was much less than the energy needed to maintain permeation. However, the flux increase at high rotational speeds at the cost of high energy consumption was not significant. This analytical approach provides insights into the techno-economic modeling of shear-enhanced systems via the use of dimensionless parameters, such as time ($t^* = tD/r^2$), shear rate ($\gamma^* = \gamma/\Omega$), flux ($J^* = J\mu R_m/\rho P$), pressure ($P^* = (P-\pi)/\pi$), permeate volume ($\mathrm{V}^* = VR_m/AP^*t^*$) and work ($\mathrm{W}^* = WR_m/AP^{*2}t^*$) (Chaudhuri and Jogdand, 2017). Similarly, Mat Nawi et al. (2022) reported that increasing the distance between the turntable and the membrane significantly decreased the flux. Encouragingly, the energy needed for rotation was two orders of magnitude lower than that needed for aeration according to the energy consumption analysis.

The self-rotation of the membrane also enables enhanced shear. Ji et al. (2016) applied a centrifugal term $\boldsymbol{S}_{m2} = \rho\omega^2\boldsymbol{r}$ in the fluid domain for a rotating tubular membrane. Rotation is particularly effective at preventing large particles from being deposited on the membrane surface but has a negligible effect on small particles ($< 8\mu$m). Pinilla et al. (2020) considered the rotation membrane in an MBR system with an eccentric placement configuration to be better than that with a central placement configuration because of its excellent ability to eliminate dead zones. The rotational speed is a key factor in wall shear stress, although moderate speeds are still recommended. There is also a positive relationship between the sludge concentration (expressed as fluid viscosity) and wall shear stress. Zhang et al. (2022) discussed the effects of rotational velocity and inlet velocity on the hydrodynamic characteristics of staggered rotating membrane systems (Fig. 6 (e)). Naskar et al. (2019) reported that the intermeshed spinning basket membrane (ISBM), which consists of two intermeshed counter rotating flat membranes (Fig. 6 (f)), is excellent for filtration at high concentrations and for severe fouling despite its high energy consumption and low space utilization. High shear stress exists at both the outer edge and near the rotational axis of the membrane surface, while areas of low shear stress exist in the middle region. The shear stress on the leading face is 1.5 times greater than that on the trailing surface.

5.4 Pulsatile flow

The primary membrane fouling control strategy produces perturbations on the membrane surface, which can be achieved by periodically changing the velocity and pressure through the application of functional feed. Measures such as pulse flow, alternating tangential flow (ATF) and the periodic feed pressure technique (PFPT) have been investigated. The function feed can be easily realized by modifying the boundary condition of the simulation domain, e.g., by assigning a periodic function to the velocity inlet or the pressure inlet.

Jalilvand et al. (2014) reported that sinusoidal pulsatile flow (u_{sin}) and step pulsatile flow (u_{uni}) have greater shear stress, which mitigates membrane fouling, than does continuous flow at the cost of affordable feed channel pressure loss (< 400 Pa/m). Li et al. (2022) further showed that step pulsatile flow exhibits better performance than sinusoidal, reciprocal and power flows. Sinusoidal pulsatile flow at 5 Hz induced greater wall shear stress and membrane flux than sinusoidal pulsatile flow at 10 Hz and continuous flow, probably because a lower frequency has a higher peak velocity to maintain the same average velocity (Li et al., 2023):

$$u_{sin} = A + A\sin\left(\frac{2\pi}{T}t + \varphi_0\right) \tag{60}$$

$$u_{\mathrm{uni}} = \begin{cases} 00 < t < T/2 \\ 2AT/2 < t < T \end{cases} \tag{61}$$

where A is the oscillation domain, T is the cycle time and φ_0 is the initial phase difference.

Radoniqi et al. (2018) developed a two-dimensional CFD model for ATF filtration considering cycle time, cross-flow rate, permeate flux and TMP. The simulation and experimental data aligned well. The Salama Team confirmed the anti-fouling capability of PEPT in a membrane system for treating oily wastewater using two-phase flow CFD simulation. Choosing the proper cycle of periodic feed pressure can interrupt the leakage process of oil droplets into membrane pores, thus slowing membrane fouling (Salama et al., 2020; Zoubeik et al., 2018).

6 Retrospection and prospection

CFD, as a versatile and extensively employed tool, plays a pivotal role in various aspects of membrane research. This work significantly contributes to hydrodynamic analysis, the establishment of fouling models, and the optimization of spacer geometry and working conditions.

Moreover, CFD enables the identification of potential areas susceptible to contamination, the formulation of precision-driven operational and cleaning methodologies, and the reduction of operational costs and energy consumption. Importantly, CFD eliminates the necessity for laborious repetitive experiments and circumvents the limitations associated with the absence of *in situ* microscopic observations. Here, we provide several suggestions for numerical simulations of fouling models and antifouling strategies:

1) It is common in simulations to choose constants as parameters for fouling models; however, these models are subject to additional constraints. For example, biomass that develops in regions of high shear stress is denser and tougher; thus, constant biomass density, porosity, and mechanical strength values are inaccurate. The deposition of inorganic crystals at the wall is influenced by hydrodynamics; therefore, a constant deposition rate is not appropriate.

2) It is necessary to experimentally obtain internal information about the fouling layer, such as the density/porosity distribution, microbial activity and foulant fraction. The above information can make an essential contribution to understanding the development of membrane fouling and improving and refining fouling models.

3) In membrane filtration systems where vibration, rotation, pulsation, and other mechanical means are used to enhance wall shear and generate wall slip, it is critical to balance the trade-offs between energy consumption and antipollution performance and to determine the optimal vibration frequency/rotation rate. CFD provides a good way to quantitatively analyze the effectiveness of antipollution agents. A model that introduces parameters such as energy consumption, shear rate, permeation flux, and CP modulus to assist in the techno-economic analysis would be very helpful.

4) Feed control methods such as pulsatile flow, alternating tangential flow (ATF) and the periodic feed pressure technique (PFPT) are promising. However, it is necessary to study the unfavorable hydraulic phenomena caused by sharp changes in the flow rate or flow direction, such as substantial pressure loss and even hydraulic shock. The cost of modifying the filtration system to achieve feed control also needs to be considered.

Acknowledgements This research was financially supported by the National Natural Science Foundation of China (No. 52270076) and the China Baowu Low Carbon Metallurgy Innovation Foundation (No. BWLCF202105).

Conflict of Interests The authors declare that the research was conducted in the absence of any commercial or financial relationships that could be construed as a potential conflict of interest.

Electronic Supplementary Material Supplementary material is available in the online version of this article at https://doi.org/10.1007/s11783-024-1853-y and is accessible for authorized users.

References

Abdelkader B A, Sharqawy M (2022). Pressure drop across membrane spacer-filled channels using porous media characteristics and computational fluid dynamics simulation. Desalination and Water Treatment, 247: 28–39

Akagi T, Horie T, Masuda H, Matsuda K, Matsumoto H, Ohmura N, Hirata Y (2018). Improvement of separation performance by fluid motion in the membrane module with a helical baffle. Separation and Purification Technology, 198: 52–59

Al-Abbasi O, Bin Shams M (2021). Dynamic CFD modelling of an industrial-scale dead-end ultrafiltration system: full cycle and complete blockage. Journal of Water Process Engineering, 40: 101887

Ali S M, Qamar A, Kerdi S, Phuntsho S, Vrouwenvelder J S, Ghaffour N, Shon H K (2019). Energy efficient 3D printed column type feed spacer for membrane filtration. Water Research, 164: 114961

Ali S M, Qamar A, Phuntsho S, Ghaffour N, Vrouwenvelder J S, Shon H K (2020). Conceptual design of a dynamic turbospacer for efficient low pressure membrane filtration. Desalination, 496: 114712

Anqi A E, Alkhamis N, Oztekin A (2015). Numerical simulation of brackish water desalination by a reverse osmosis membrane. Desalination, 369: 156–164

Araújo P A, Kruithof J C, Van Loosdrecht M C M, Vrouwenvelder J S (2012). The potential of standard and modified feed spacers for biofouling control. Journal of Membrane Science, 403–404: 58–70

Asadollahi M, Bastani D, Musavi S A (2017). Enhancement of surface properties and performance of reverse osmosis membranes after surface modification: a review. Desalination, 420: 330–383

Bae S, Gu B, Lee J H (2023). A 3D CFD study on the effects of feed spacer designs on membrane performance for high-permeance RO membranes. Journal of Water Process Engineering, 53: 103887

Bahoosh M, Kashi E, Shokrollahzadeh S (2022). The side stream and different spacers effects on the permeate water flux in forward osmosis process using computational fluid dynamics. Chemical Engineering and Processing, 181: 109113

Binger Z M, Achilli A (2023). Surrogate modeling of pressure loss & mass transfer in membrane channels via coupling of computational fluid dynamics and machine learning. Desalination, 548: 116241

Boudinar M B, Hanbury W T, Avlonitis S (1992). Numerical simulation and optimisation of spiral-wound modules. Desalination, 86(3): 273–290

Boudreau B P (1996). The diffusive tortuosity of fine-grained unlithified sediments. Geochimica et Cosmochimica Acta, 60(16): 3139–3142

Bräsel B, Yoo S W, Huber S, Wessling M, Linkhorst J (2023). Evolution of particle deposits at communicating membrane pores during crossflow filtration. Journal of Membrane Science, 686: 121977

Brinkman H C (1949). A calculation of the viscous force exerted by a

flowing fluid on a dense swarm of particles. Flow, Turbulence and Combustion, 1(1): 27–34

Bucs S S, Farhat N, Kruithof J C, Picioreanu C, van Loosdrecht M C M, Vrouwenvelder J S (2018). Review on strategies for biofouling mitigation in spiral wound membrane systems. Desalination, 434: 189–197

Bucs S S, Valladares Linares R, Marston J O, Radu A I, Vrouwenvelder J S, Picioreanu C (2015). Experimental and numerical characterization of the water flow in spacer-filled channels of spiral-wound membranes. Water Research, 87: 299–310

Bucs S S, Valladares Linares R, Vrouwenvelder J S, Picioreanu C (2016). Biofouling in forward osmosis systems: an experimental and numerical study. Water Research, 106: 86–97

Bucs Sz S, Radu A I, Lavric V, Vrouwenvelder J S, Picioreanu C (2014a). Effect of different commercial feed spacers on biofouling of reverse osmosis membrane systems: a numerical study. Desalination, 343: 26–37

Bucs Sz S, Valladares Linares R, van Loosdrecht M C M, Kruithof J C, Vrouwenvelder J S (2014b). Impact of organic nutrient load on biomass accumulation, feed channel pressure drop increase and permeate flux decline in membrane systems. Water Research, 67: 227–242

Cao H, O'Rourke M, Habimana O, Casey E (2018). Analysis of surrogate bacterial cell transport to nanofiltration membranes: effect of salt concentration and hydrodynamics. Separation and Purification Technology, 207: 498–505

Cao Z (2001). CFD simulations of net-type turbulence promoters in a narrow channel. Journal of Membrane Science, 185(2): 157–176

Carman P C (1997). Fluid flow through granular beds. Chemical Engineering Research & Design, 75: S32–S48

Chaudhuri A, Jogdand A (2017). Permeate flux decrease due to concentration polarization in a closed roto-dynamic reverse osmosis filtration system. Desalination, 402: 152–161

Choi D C, Jung S Y, Won Y J, Jang J H, Lee J, Chae H R, Ahn K H, Lee S, Park P K, Lee C H (2015). Three-dimensional hydraulic modeling of particle deposition on the patterned isopore membrane in crossflow microfiltration. Journal of Membrane Science, 492: 156–163

Chong T H, Wong F S, Fane A G (2008). The effect of imposed flux on biofouling in reverse osmosis: role of concentration polarisation and biofilm enhanced osmotic pressure phenomena. Journal of Membrane Science, 325(2): 840–850

Chong Y K, Liang Y Y, Lau W J, Fimbres Weihs G A (2022). 3D CFD study of hydrodynamics and mass transfer phenomena for spiral wound membrane submerged-type feed spacer with different node geometries and sizes. International Journal of Heat and Mass Transfer, 191: 122819

Chong Y K, Liang Y Y, Weihs G A F (2023). Validation and characterisation of mass transfer of 3D-CFD model for twisted feed spacer. Desalination, 554: 116516

Chun Y, Jeong K, Cho K H (2020). Influences of combined organic fouling and inorganic scaling on flux and fouling behaviors in forward osmosis. Membranes, 10(6): 115

Completo C, Semiao V, Geraldes V (2016). Efficient CFD-based method for designing cross-flow nanofiltration small devices. Journal of Membrane Science, 500: 190–202

Desmond P, Huisman K T, Sanawar H, Farhat N M, Traber J, Fridjonsson E O, Johns M L, Flemming H C, Picioreanu C, Vrouwenvelder J S (2022). Controlling the hydraulic resistance of membrane biofilms by engineering biofilm physical structure. Water Research, 210: 118031

Dydo P, Turek M, Ciba J, Wandachowicz K, Misztal J (2004). The nucleation kinetic aspects of gypsum nanofiltration membrane scaling. Desalination, 164(1): 41–52

Evangelista F (1988). An improved analytical method for the design of spiral-wound modules. Chemical Engineering Journal, 38(1): 33–40

Fang H H, Wu R M (2008). Determination of hydrodynamic shear force exerted on membrane surface in cross-flow filtration by multiphase flow simulation. Journal of Chemical Engineering of Japan, 41(10): 961–966

Fimbres-Weihs G A, Wiley D E (2007). Numerical study of mass transfer in three-dimensional spacer-filled narrow channels with steady flow. Journal of Membrane Science, 306(1–2): 228–243

Fimbres Weihs G A, Wiley D E (2014). CFD analysis of tracer response technique under cake-enhanced osmotic pressure. Journal of Membrane Science, 449: 38–49

Fowler J D, Robertson C R (1991). Hydraulic permeability of immobilized bacterial cell aggregates. Applied and Environmental Microbiology, 57(1): 102–113

Gao Y, Haavisto S, Tang C Y, Salmela J, Li W (2013). Characterization of fluid dynamics in spacer-filled channels for membrane filtration using Doppler optical coherence tomography. Journal of Membrane Science, 448: 198–208

García-Picazo F J, Fletcher D F, Fimbres-Weihs G A (2023). Mass transfer enhancement in spacer-filled membrane channels by flow oscillation induced vortex shedding: Numerical study of the effect of amplitude. International Journal of Heat and Mass Transfer, 209: 124054

Goh P S, Lau W J, Othman M H D, Ismail A F (2018). Membrane fouling in desalination and its mitigation strategies. Desalination, 425: 130–155

Goh P S, Zulhairun A K, Ismail A F, Hilal N (2019). Contemporary antibiofouling modifications of reverse osmosis desalination membrane: a review. Desalination, 468: 114072

Gorzalski A S, Coronell O (2014). Fouling of nanofiltration membranes in full- and bench-scale systems treating groundwater containing silica. Journal of Membrane Science, 468: 349–359

Gu B, Adjiman C S, Xu X Y (2017). The effect of feed spacer geometry on membrane performance and concentration polarisation based on 3D CFD simulations. Journal of Membrane Science, 527: 78–91

Gu B, Adjiman C S, Xu X Y (2021). Correlations for concentration polarization and pressure drop in spacer-filled RO membrane modules based on CFD simulations. Membranes, 11(5): 338

Guan H, Lin P, Yu S, Hu X, Li X, Zhu Z (2023). Hydrodynamic effects of non-uniform feed spacer structures on energy loss and mass transfer in spiral wound module. Journal of Membrane Science, 673: 121479

Guillen G, Hoek E M V (2009). Modeling the impacts of feed spacer geometry on reverse osmosis and nanofiltration processes. Chemical Engineering Journal, 149(1–3): 221–231

Haidari A H, Heijman S G J, van der Meer W G J (2018). Optimal

design of spacers in reverse osmosis. Separation and Purification Technology, 192: 441–456

Han Z, Terashima M, Liu B, Yasui H (2018). CFD investigation of the effect of the feed spacer on hydrodynamics in spiral wound membrane modules. Mathematical and Computational Applications, 23(4): 80

Hwang K J, Lin S J (2014). Filtration flux-shear stress-cake mass relationships in microalgae rotating-disk dynamic microfiltration. Chemical Engineering Journal, 244: 429–437

Ilyas A, Mertens M, Oyaert S, Vankelecom I F J (2021). Anti-fouling behavior of micro-patterned PVDF membranes prepared via spray-assisted phase inversion: influence of pattern shapes and flow configuration. Separation and Purification Technology, 259: 118041

Ilyas A, Timmermans L, Vanierschot M, Smets I, Vankelecom I F J (2022). Micro-patterned PVDF membranes and magnetically induced membrane vibration system for efficient membrane bioreactor operation. Journal of Membrane Science, 662: 120978

Jafari M, Desmond P, van Loosdrecht M C M, Derlon N, Morgenroth E, Picioreanu C (2018). Effect of biofilm structural deformation on hydraulic resistance during ultrafiltration: a numerical and experimental study. Water Research, 145: 375–387

Jalilvand Z, Zokaee Ashtiani F, Fouladitajar A, Rezaei H (2014). Computational fluid dynamics modeling and experimental study of continuous and pulsatile flow in flat sheet microfiltration membranes. Journal of Membrane Science, 450: 207–214

Jamieson T, Leterme S C (2021). Influences and impacts of biofouling in SWRO desalination plants. Critical Reviews in Environmental Science and Technology, 51(12): 1281–1301

Janus T (2014). Integrated Mathematical Model of a MBR Reactor Including Biopolymer Kinetics and Membrane Fouling. Procedia Engineering, 12th International Conference on Computing and Control for the Water Industry, CCWI2013 70: 882–891

Janus T, Ulanicki B. (2015). ASM1-Based Activated Sludge Model with Biopolymer Kinetics for Integrated Simulation of Membrane Bioreactors for Wastewater Treatment. Procedia Engineering, Computing and Control for the Water Industry (CCWI2015) Sharing the Best Practice in Water Management 119: 1318–1327

Jeong K, Park M, Oh S, Kim J H (2020). Impacts of flow channel geometry, hydrodynamic and membrane properties on osmotic backwash of RO membranes—CFD modeling and simulation. Desalination, 476: 114229

Ji P, Motin A, Shan W, Bénard A, Bruening M L, Tarabara V V (2016). Dynamic crossflow filtration with a rotating tubular membrane: using centripetal force to decrease fouling by buoyant particles. Chemical Engineering Research & Design, 106: 101–114

Jogdand A, Chaudhuri A (2015). Modeling of concentration polarization and permeate flux variation in a roto-dynamic reverse osmosis filtration system. Desalination, 375: 54–70

Johnston J, Dischinger S M, Nassr M, Lee J Y, Bigdelou P, Freeman B D, Gleason K L, Martinand D, Miller D J, Molins S, et al. (2023). A reduced-order model of concentration polarization in reverse osmosis systems with feed spacers. Journal of Membrane Science, 675: 121508

Johnston J, Lou J, Tilton N (2022). Application of projection methods to simulating mass transport in reverse osmosis systems. Computers & Fluids, 232: 105189

Jung S Y, Ahn K H (2019). Transport and deposition of colloidal particles on a patterned membrane surface: effect of cross-flow velocity and the size ratio of particle to surface pattern. Journal of Membrane Science, 572: 309–319

Karabelas A J, Kostoglou M, Koutsou C P (2015). Modeling of spiral wound membrane desalination modules and plants: review and research priorities. Desalination, 356: 165–186

Kavianipour O, Ingram G D, Vuthaluru H B (2017). Investigation into the effectiveness of feed spacer configurations for reverse osmosis membrane modules using computational fluid dynamics. Journal of Membrane Science, 526: 156–171

Kavianipour O, Ingram G D, Vuthaluru H B (2019). Studies into the mass transfer and energy consumption of commercial feed spacers for RO membrane modules using CFD: effectiveness of performance measures. Chemical Engineering Research & Design, 141: 328–338

Kerdi S, Qamar A, Alpatova A, Vrouwenvelder J S, Ghaffour N (2020). Membrane filtration performance enhancement and biofouling mitigation using symmetric spacers with helical filaments. Desalination, 484: 114454

Kerdi S, Qamar A, Vrouwenvelder J S, Ghaffour N (2018). Fouling resilient perforated feed spacers for membrane filtration. Water Research, 140: 211–219

Kerdi S, Qamar A, Vrouwenvelder J S, Ghaffour N (2021). Effect of localized hydrodynamics on biofilm attachment and growth in a cross-flow filtration channel. Water Research, 188: 116502

Keucken A, Liu X, Lian B, Wang Y, Persson K M, Leslie G (2018). Simulation of NOM removal by capillary NF: a numerical method for full-scale plant design. Journal of Membrane Science, 555: 229–236

Kim K, Jung J Y, Kwon J H, Yang J W (2015). Dynamic microfiltration with a perforated disk for effective harvesting of microalgae. Journal of Membrane Science, 475: 252–258

Knutsen J S, Davis R H (2006). Deposition of foulant particles during tangential flow filtration. Journal of Membrane Science, 271(1–2): 101–113

Kostoglou M, Karabelas A J (2013). Comprehensive simulation of flat-sheet membrane element performance in steady state desalination. Desalination, 316: 91–102

Koutsou C P, Karabelas A J (2015). A novel retentate spacer geometry for improved spiral wound membrane (SWM) module performance. Journal of Membrane Science, 488: 129–142

Koutsou C P, Karabelas A J, Kostoglou M (2018). Fluid dynamics and mass transfer in spacer-filled membrane channels: effect of uniform channel-gap reduction due to fouling. Fluids, 3(1): 12

Koutsou C P, Yiantsios S G, Karabelas A J (2007). Direct numerical simulation of flow in spacer-filled channels: effect of spacer geometrical characteristics. Journal of Membrane Science, 291(1–2): 53–69

Koutsou C P, Yiantsios S G, Karabelas A J (2009). A numerical and experimental study of mass transfer in spacer-filled channels: effects of spacer geometrical characteristics and Schmidt number. Journal of Membrane Science, 326(1): 234–251

Lecuyer S, Rusconi R, Shen Y, Forsyth A, Vlamakis H, Kolter R, Stone H A (2011). Shear stress increases the residence time of

adhesion of pseudomonas aeruginosa. Biophysical Journal, 100(2): 341–350

Lee Y K, Won Y J, Yoo J H, Ahn K H, Lee C H (2013). Flow analysis and fouling on the patterned membrane surface. Journal of Membrane Science, 427: 320–325

Li B, Dobosz K M, Zhang H, Schiffman J D, Saranteas K, Henson M A (2019). Predicting the performance of pressure filtration processes by coupling computational fluid dynamics and discrete element methods. Chemical Engineering Science, 208: 115162

Li C, Zhang D, Liu J, Xiong H, Sun T, Wu X, Shi Z, Lin Q (2022). Study on the control of membrane fouling by pulse function feed and CFD simulation verification. Membranes, 12(4): 362

Li F, Meindersma W, de Haan A B, Reith T (2004). Experimental validation of CFD mass transfer simulations in flat channels with non-woven net spacers. Journal of Membrane Science, 232(1–2): 19–30

Li J, Xu C, Ye J, Li E, Xu S, Huang M (2023). Enhanced anti-fouling of forward osmosis membrane by pulsatile flow operation in textile wastewater treatment. Desalination, 565: 116878

Li M, Bui T, Chao S (2016). Three-dimensional CFD analysis of hydrodynamics and concentration polarization in an industrial RO feed channel. Desalination, 397: 194–204

Li X, Wang X (2006). Modelling of membrane fouling in a submerged membrane bioreactor. Journal of Membrane Science, 278(1–2): 151–161

Li Y L, Tung K L (2008). CFD simulation of fluid. flow through spacer-filled membrane module: selecting suitable cell types for periodic boundary conditions. Desalination, 233(1–3): 351–358

Liang Y Y, Fimbres Weihs G A, Wiley D E (2020). Comparison of oscillating flow and slip velocity mass transfer enhancement in spacer-filled membrane channels: CFD analysis and validation. Journal of Membrane Science, 593: 117433

Liang Y Y, Fletcher D F (2023). Computational fluid dynamics simulation of forward osmosis (FO) membrane systems: methodology, state of art, challenges and opportunities. Desalination, 549: 116359

Liang Y Y, Toh K Y, Fimbres Weihs G A (2019). 3D CFD study of the effect of multi-layer spacers on membrane performance under steady flow. Journal of Membrane Science, 580: 256–267

Lin W, Lei J, Wang Q, Wang X M, Huang X (2022a). Performance enhancement of spiral-wound reverse osmosis membrane elements with novel diagonal-flow feed channels. Desalination, 523: 115447

Lin W, Li D, Wang Q, Wang X, Huang X (2023). Dynamic evolution of membrane biofouling in feed channels affected by spacer–membrane clearance and the induced hydrodynamic conditions. Journal of Membrane Science, 668: 121209

Lin W, Shao R, Wang X, Huang X (2020). Impacts of non-uniform filament feed spacers characteristics on the hydraulic and anti-fouling performances in the spacer-filled membrane channels: experiment and numerical simulation. Water Research, 185: 116251

Lin W, Wang Q, Sun L, Wang D, Cabrera J, Li D, Hu L, Jiang G, Wang X, Huang X (2022b). The critical role of feed spacer channel porosity in membrane biofouling: insights and implications. Journal of Membrane Science, 649: 120395

Lin W, Zhang Y, Li D, Wang X, Huang X (2021). Roles and performance enhancement of feed spacer in spiral wound membrane modules for water treatment: a 20-year review on research evolvement. Water Research, 198: 117146

Lohaus J, Perez Y M, Wessling M (2018). What are the microscopic events of colloidal membrane fouling? Journal of Membrane Science, 553: 90–98

Lorente E, Haponska M, Clavero E, Torras C, Salvado J (2018). Steam explosion and vibrating membrane filtration to improve the processing cost of microalgae cell disruption and fractionation. Processes, 6(4): 28

Luo J, Li M, Heng Y (2020). A hybrid modeling approach for optimal design of non-woven membrane channels in brackish water reverse osmosis process with high-throughput computation. Desalination, 489: 114463

Luo L W, Wu Y H, Chen G Q, Wang H B, Wang Y H, Tong X, Bai Y, Xu Y Q, Zhang Z W, Ikuno N, et al. (2022). Chlorine-resistant bacteria (CRB) in the reverse osmosis system for wastewater reclamation: isolation, identification and membrane fouling mechanisms. Water Research, 209: 117966

Ma C, Liu Y, Li F, Shen C, Huang M, Wang Z, Cao C, Zhou Q, Sheng Y, Sand W (2019). CFD simulations of fiber-fiber interaction in a hollow fiber membrane bundle: fiber distance and position matters. Separation and Purification Technology, 209: 707–713

Mao W, Zou X, Guo Z, Sun S, Ma S, Lyv S, Xiao Y, Ji X, Wang Y (2021). Numerical simulations of calcium sulphate scaling in full-scale brackish water reverse osmosis pressure vessels using computational fluid dynamics. Membranes, 11(7): 521

Mat Nawi N I, Mohd Lazis A, Rahma A, Elma M, Bilad M R, Md Nordin N A H, Wirzal M D H, Shamsuddin N, Suhaimi H, Yusof N (2022). A rotary spacer system for energy-efficient membrane fouling control in oil/water emulsion filtration. Membranes, 12(6): 554

McDonogh R, Schaule G, Flemming H C (1994). The permeability of biofouling layers on membranes. Journal of Membrane Science, 87(1–2): 199–217

Mohan T R, Mohan Kumar M S, Rao L (2022). Biofouling of hollow fiber ultrafiltration membranes: a novel multiphase CFD–Porous-CES model and experimental study. Journal of Membrane Science, 663: 121034

Mokhtar I E, Gurreri L, Tamburini A, Cipollina A, Ciofalo M, Bouguecha S, Micale G (2021). CFD prediction of flow, heat and mass transfer in woven spacer-filled channels for membrane processes. International Journal of Heat and Mass Transfer, 173: 121246

Monod J (1941). Growth of bacterial populations in function of concentration of a hydrocarbon diet. Comptes Rendus Hebdomadaires Sciences, 212: 771–773

Movahedi H, Jamshidi S (2022). New insight into hydrodynamic and cake erosion mechanism during rotating-disk dynamic microfiltration of concentrated bentonite suspensions at different salinity conditions. Separation and Purification Technology, 300: 121844

Najid N, Hakizimana J N, Kouzbour S, Gourich B, Ruiz-García A, Vial C, Stiriba Y, Semiat R (2022). Fouling control and modeling in reverse osmosis for seawater desalination: a review. Computers & Chemical Engineering, 162: 107794

Naskar M, Rana K, Chatterjee D, Dhara T, Sultana R, Sarkar D (2019).

Design, performance characterization and hydrodynamic modeling of intermeshed spinning basket membrane (ISBM) module. Chemical Engineering Science, 206: 446–462

Ndinisa N V, Wiley D E, Fletcher D F (2005). Computational fluid dynamics simulations of taylor bubbles in tubular membranes: model validation and application to laminar flow systems. Chemical Engineering Research & Design, 83(1): 40–49

Olivera-Nappa A, Picioreanu C, Asenjo J A (2010). Non-homogeneous biofilm modeling applied to bioleaching processes. Biotechnology and Bioengineering, 106(4): 660–676

Park H G, Cho S G, Kim K J, Kwon Y N (2016). Effect of feed spacer thickness on the fouling behavior in reverse osmosis process: a pilot scale study. Desalination, 379: 155–163

Park J E, Kang T G, Moon H (2023). The effect of the rotating disk geometry on the flow and flux enhancement in a dynamic filtration system. Membranes, 13(3): 291

Park S, Jeong Y D, Lee J H, Kim J, Jeong K, Cho K H (2021). 3D printed honeycomb-shaped feed channel spacer for membrane fouling mitigation in nanofiltration. Journal of Membrane Science, 620: 118665

Petrosino F, De Luca G, Curcio S, Wickramasinghe S R, Chakraborty S (2023). Micro-CFD modelling of ultrafiltration bio-fouling. Separation Science and Technology, 58(1): 131–140

Picioreanu C, Blauert F, Horn H, Wagner M (2018). Determination of mechanical properties of biofilms by modelling the deformation measured using optical coherence tomography. Water Research, 145: 588–598

Picioreanu C, Kreft J U, Van Loosdrecht M C M (2004). Particle-based multidimensional multispecies biofilm model. Applied and Environmental Microbiology, 70(5): 3024–3040

Picioreanu C, van Loosdrecht M C, Heijnen J J (1998a). Mathematical modeling of biofilm structure with a hybrid differential-discrete cellular automaton approach. Biotechnology and Bioengineering, 58(1): 101–116

Picioreanu C, van Loosdrecht M C, Heijnen J J (1998b). A new combined differential-discrete cellular automaton approach for biofilm modeling: application for growth in gel beads. Biotechnology and Bioengineering, 57(6): 718–731

Picioreanu C, van Loosdrecht M C, Heijnen J J (2001). Two-dimensional model of biofilm detachment caused by internal stress from liquid flow. Biotechnology and Bioengineering, 72(2): 205–218

Picioreanu C, Vrouwenvelder J S, van Loosdrecht M C M (2009). Three-dimensional modeling of biofouling and fluid dynamics in feed spacer channels of membrane devices. Journal of Membrane Science, 345(1–2): 340–354

Pinilla A, Berrio J C, Guerrero E, Valdés J P, Becerra D, Pico P, Vargas L, Madsen S, Bentzen T R, Ratkovich N (2020). CFD modelling of the hydrodynamics in a filtration unit with rotating membranes. Journal of Water Process Engineering, 36: 101368

Piyadasa C, Ridgway H F, Yeager T R, Stewart M B, Pelekani C, Gray S R, Orbell J D (2017). The application of electromagnetic fields to the control of the scaling and biofouling of reverse osmosis membranes: a review. Desalination, 418: 19–34

Prakash N, Chaudhuri A, Das S P (2023). Numerical modelling and analysis of concentration polarization and scaling of gypsum over RO membrane during seawater desalination. Chemical Engineering Research & Design, 190: 497–507

Puderbach V, Schmidt K, Antonyuk S (2021). A coupled CFD-DEM model for resolved simulation of filter cake formation during solid-liquid separation. Processes, 9(5): 826

Qamar A, Bucs S, Picioreanu C, Vrouwenvelder J, Ghaffour N (2019). Hydrodynamic flow transition dynamics in a spacer filled filtration channel using direct numerical simulation. Journal of Membrane Science, 590: 117264

Qamar A, Kerdi S, Ali S M, Shon H K, Vrouwenvelder J S, Ghaffour N (2021). Novel hole-pillar spacer design for improved hydrodynamics and biofouling mitigation in membrane filtration. Scientific Reports, 11(1): 6979

Radoniqi F, Zhang H, Bardliving C L, Shamlou P, Coffman J (2018). Computational fluid dynamic modeling of alternating tangential flow filtration for perfusion cell culture. Biotechnology and Bioengineering, 115(11): 2751–2759

Radu A I, Bergwerff L, van Loosdrecht M C M, Picioreanu C (2014a). A two-dimensional mechanistic model for scaling in spiral wound membrane systems. Chemical Engineering Journal, 241: 77–91

Radu A I, Bergwerff L, van Loosdrecht M C M, Picioreanu C (2015). Combined biofouling and scaling in membrane feed channels: a new modeling approach. Biofouling, 31(1): 83–100

Radu A I, van Steen M S H, Vrouwenvelder J S, van Loosdrecht M C M, Picioreanu C (2014b). Spacer geometry and particle deposition in spiral wound membrane feed channels. Water Research, 64: 160–176

Radu A I, Vrouwenvelder J S, van Loosdrecht M C M, Picioreanu C (2010). Modeling the effect of biofilm formation on reverse osmosis performance: flux, feed channel pressure drop and solute passage. Journal of Membrane Science, 365(1–2): 1–15

Radu A I, Vrouwenvelder J S, van Loosdrecht M C M, Picioreanu C (2012). Effect of flow velocity, substrate concentration and hydraulic cleaning on biofouling of reverse osmosis feed channels. Chemical Engineering Journal, 188: 30–39

Rahimi M, Madaeni S S, Abolhasani M, Alsairafi A A (2009). CFD and experimental studies of fouling of a microfiltration membrane. Chemical Engineering and Processing, 48(9): 1405–1413

Rahmawati R, Bilad M R, Nawi N I M, Wibisono Y, Suhaimi H, Shamsuddin N, Arahman N (2021). Engineered spacers for fouling mitigation in pressure driven membrane processes: progress and projection. Journal of Environmental Chemical Engineering, 9(5): 106285

Rajabzadeh A R, Moresoli C, Marcos B (2010). Fouling behavior of electroacidified soy protein extracts during cross-flow ultrafiltration using dynamic reversible-irreversible fouling resistances and CFD modeling. Journal of Membrane Science, 361(1–2): 191–205

Ruiz-García A, de la Nuez Pestana I (2019). Feed spacer geometries and permeability coefficients: effect on the performance in BWRO spriral-wound membrane modules. Water, 11(1): 152

Sablani S, Goosen M, Al-Belushi R, Wilf M (2001). Concentration polarization in ultrafiltration and reverse osmosis: a critical review. Desalination, 141(3): 269–289

Saeed A, Vuthaluru R, Yang Y, Vuthaluru H B (2012). Effect of feed spacer arrangement on flow dynamics through spacer filled membranes. Desalination, 285: 163–169

Salama A, Zoubeik M, Henni A, Ng K T W, Ibrahim H (2020). On the design of sustainable antifouling system for the crossflow filtration of oily water systems: a multicontinuum and CFD investigation of the periodic feed pressure technique. Science of the Total Environment, 698: 134288

Saur T, Morin E, Habouzit F, Bernet N, Escudié R (2017). Impact of wall shear stress on initial bacterial adhesion in rotating annular reactor. PLoS One, 12(2): e0172113

Schausberger P, Norazman N, Li H, Chen V, Friedl A (2009). Simulation of protein ultrafiltration using CFD: comparison of concentration polarisation and fouling effects with filtration and protein adsorption experiments. Journal of Membrane Science, 337(1–2): 1–8

Schock G, Miquel A (1987). Mass transfer and pressure loss in spiral wound modules. Desalination, 64: 339–352

Schwinge J, Wiley D E, Fane A G (2004). Novel spacer design improves observed flux. Journal of Membrane Science, 229(1–2): 53–61

Schwinge J, Wiley D E, Fletcher D F (2002a). Simulation of the flow around spacer filaments between channel walls. 2. Mass-transfer enhancement. Industrial & Engineering Chemistry Research, 41(19): 4879–4888

Schwinge J, Wiley D E, Fletcher D F (2002b). Simulation of the flow around spacer filaments between narrow channel walls. 1. Hydrodynamics. Industrial & Engineering Chemistry Research, 41(12): 2977–2987

Senthilmurugan S, Ahluwalia A, Gupta S K (2005). Modeling of a spiral-wound module and estimation of model parameters using numerical techniques. Desalination, 173(3): 269–286

Shakaib M, Hasani S M F, Mahmood M (2007). Study on the effects of spacer geometry in membrane feed channels using three-dimensional computational flow modeling. Journal of Membrane Science, 297(1–2): 74–89

Shang C, Pranantyo D, Zhang S (2020a). Understanding the roughness–fouling relationship in reverse osmosis: mechanism and implications. Environmental Science & Technology, 54(8): 5288–5296

Shang C, Wang L, Xia J, Zhang S (2020b). Macropatterning of microcrumpled nanofiltration membranes by spacer imprinting for low-scaling desalination. Environmental Science & Technology, 54(23): 15527–15533

Shang C, Xia J, Sun L, Lipscomb G G, Zhang S (2022a). Concentration polarization on surface patterned membranes. AIChE Journal. American Institute of Chemical Engineers, 68(12): e17832

Shang W, Li X, Liu W, Yue S, Li M, von Eiff D, Sun F, An A K (2021). Effective suppression of concentration polarization by nanofiltration membrane surface pattern manipulation: numerical modeling based on LIF visualization. Journal of Membrane Science, 622: 119021

Shang W, Yang S, Liu W, Wong P W, Wang R, Li X, Sheng G, Lau W, An A K, Sun F (2022b). Understanding the influence of hydraulic conditions on colloidal fouling development by using the micro-patterned nanofiltration membrane: experiments and numerical simulation. Journal of Membrane Science, 654: 120559

Sheikholeslami R, Ong H W K (2003). Kinetics and thermodynamics of calcium carbonate and calcium sulfate at salinities up to 1.5 M. Desalination, Desalination and the Environment, 157(1): 217–234

Singh C P, Yadav A, Kumar A (2022). Numerical simulations of the effect of spacer filament geometry and orientation on the performance of the reverse osmosis process. Colloids and Surfaces. A, Physicochemical and Engineering Aspects, 650: 129664

Sioutopoulos D C, Karabelas A J (2012). Correlation of organic fouling resistances in RO and UF membrane filtration under constant flux and constant pressure. Journal of Membrane Science, 407–408: 34–46

Sitaraman H, Battiato I (2022). Impact of large-scale effects on mass transfer and concentration polarization in reverse osmosis membrane systems. Separation and Purification Technology, 303: 122121

Su X, Li W, Palazzolo A, Ahmed S (2018). Concentration polarization and permeate flux variation in a vibration enhanced reverse osmosis membrane module. Desalination, 433: 75–88

Su X, Li W, Palazzolo A, Ahmed S (2019). Permeate flux increase by colloidal fouling control in a vibration enhanced reverse osmosis membrane desalination system. Desalination, 453: 22–36

Sutariya B, Sargaonkar A, Markam B K, Raval H (2022). 3D CFD study and optimisation of static mixer type feed spacer for reverse osmosis. Chemical Engineering Journal Advances, 11: 100335

Sweity A, Oren Y, Ronen Z, Herzberg M (2013). The influence of antiscalants on biofouling of RO membranes in seawater desalination. Water Research, 47(10): 3389–3398

Tan Y Z, Mao Z, Zhang Y, Tan W S, Chong T H, Wu B, Chew J W (2019). Enhancing fouling mitigation of submerged flat-sheet membranes by vibrating 3D-spacers. Separation and Purification Technology, 215: 70–80

Thompson J, Lin N, Lyster E, Arbel R, Knoell T, Gilron J, Cohen Y (2012). RO membrane mineral scaling in the presence of a biofilm. Journal of Membrane Science, 415–416: 181–191

Toh K Y, Liang Y Y, Lau W J, Fimbres Weihs G A (2020). 3D CFD study on hydrodynamics and mass transfer phenomena for SWM feed spacer with different floating characteristics. Chemical Engineering Research & Design, 159: 36–46

Tsai H Y, Huang A, Soesanto J F, Luo Y L, Hsu T Y, Chen C H, Hwang K J, Ho CD, Tung K L (2019). 3D printing design of turbulence promoters in a cross-flow microfiltration system for fine particles removal. Journal of Membrane Science 573: 647–656. .

Uppu A, Chaudhuri A, Das S P, Prakash N (2020). CFD modeling of gypsum scaling in cross-flow RO filters using moments of particle population balance. Journal of Environmental Chemical Engineering, 8(5): 104151

Uppu A, Chaudhuri A, Prasad Das S (2019). Numerical modeling of particulate fouling and cake-enhanced concentration polarization in roto-dynamic reverse osmosis filtration systems. Desalination, 468: 114053

Vrouwenvelder J S, Graf von der Schulenburg D A, Kruithof J C, Johns M L, van Loosdrecht M C M (2009a). Biofouling of spiral-wound nanofiltration and reverse osmosis membranes: a feed spacer problem. Water Research, 43(3): 583–594

Vrouwenvelder J S, Hinrichs C, van der Meer W G J, van Loosdrecht M C M, Kruithof J C (2009b). Pressure drop increase by biofilm accumulation in spiral wound RO and NF membrane systems: role of substrate concentration, flow velocity, substrate load and flow

direction. Biofouling, 25(6): 543–555

Vrouwenvelder J S, van Paassen J A M, van Agtmaal J M C, van Loosdrecht M C M, Kruithof J C (2009c). A critical flux to avoid biofouling of spiral wound nanofiltration and reverse osmosis membranes: fact or fiction? Journal of Membrane Science, 326(1): 36–44

Wang H, Sodagari M, Ju L K, Zhang Newby B (2013). Effects of shear on initial bacterial attachment in slow flowing systems. Colloids and Surfaces. B, Biointerfaces, 109: 32–39

Wang Q, Lin W, Chou S, Dai P, Huang X (2023). Patterned membranes for improving hydrodynamic properties and mitigating membrane fouling in water treatment: a review. Water Research, 236: 119943

Wei W, Zou X, Ji X, Zhou R, Zhao K, Wang Y (2021). Analysis of concentration polarisation in full-size spiral wound reverse osmosis membranes using computational fluid dynamics. Membranes, 11(5): 353

Won Y J, Jung S Y, Jang J H, Lee J W, Chae H R, Choi D C, Hyun Ahn K, Lee C H, Park P K (2016). Correlation of membrane fouling with topography of patterned membranes for water treatment. Journal of Membrane Science, 498: 14–19

Wu R M, Lin Y J (2012). Tubular membrane filtration with a side stream and its intermittent backwash operation. Separation Science and Technology, 47(12): 1689–1697

Xie P, Murdoch L C, Ladner D A (2014). Hydrodynamics of sinusoidal spacers for improved reverse osmosis performance. Journal of Membrane Science, 453: 92–99

Xie P, Murdoch L C, Ladner D A (2019). Mitigating membrane fouling with sinusoidal spacers. Desalination and Water Treatment, 168: 56–64

Xie X, Le Men C, Dietrich N, Schmitz P, Fillaudeau L (2018). Local hydrodynamic investigation by PIV and CFD within a Dynamic filtration unit under laminar flow. Separation and Purification Technology, 198: 38–51

Yang S, Shang W, Shi H, Sun F, Zeng H (2023). Development of an automatic and object-oriented method for spacer design in the spiral wound nanofiltration modules to comprehensively enhance filtration performance. Desalination, 566: 116945

Zamani F, Law A W K, Fane A G (2013). Hydrodynamic analysis of vibrating hollow fibre membranes. Journal of Membrane Science, 429: 304–312

Zhang T, Klapper I (2010). Mathematical model of biofilm induced calcite precipitation. Water Science and Technology, 61(11): 2957–2964

Zhang W, Liang W, Xie X (2022). Computational fluid dynamic simulation for hydrodynamic shear enhanced filtration in multiple shaft disk filtration system. Journal of Water Process Engineering, 49: 103165

Zhao Z, Ilyas A, Muylaert K, Vankelecom I F J (2020). Optimization of patterned polysulfone membranes for microalgae harvesting. Bioresource Technology, 309: 123367

Zhao Z, Muylaert K, Szymczyk A, Vankelecom I F J (2021). Harvesting microalgal biomass using negatively charged polysulfone patterned membranes: influence of pattern shapes and mechanism of fouling mitigation. Water Research, 188: 116530

Zhou Z, Ling B, Battiato I, Husson S M, Ladner D A (2021). Concentration polarization over reverse osmosis membranes with engineered surface features. Journal of Membrane Science, 617: 118199

Zhuang L, Dai G, Xu Z L (2018). Three-dimensional simulation of the time-dependent fluid flow and fouling behavior in an industrial hollow fiber membrane module. AIChE Journal. American Institute of Chemical Engineers, 64(7): 2655–2669

Zoubeik M, Salama A, Henni A (2018). A novel antifouling technique for the crossflow filtration using porous membranes: experimental and CFD investigations of the periodic feed pressure technique. Water Research, 146: 159–176